D3.4 – Report on H_2 fuel gas characteristics and flow measurement

Elsa Busson, Lukas Sankowski
RWTH Aachen University - IOB

Carolin Lohrberg, Martin Oberländer
Endress+Hauser SICK GmbH & Co.KG (formerly SICK Engineering GmbH) - SIEN

December 2024

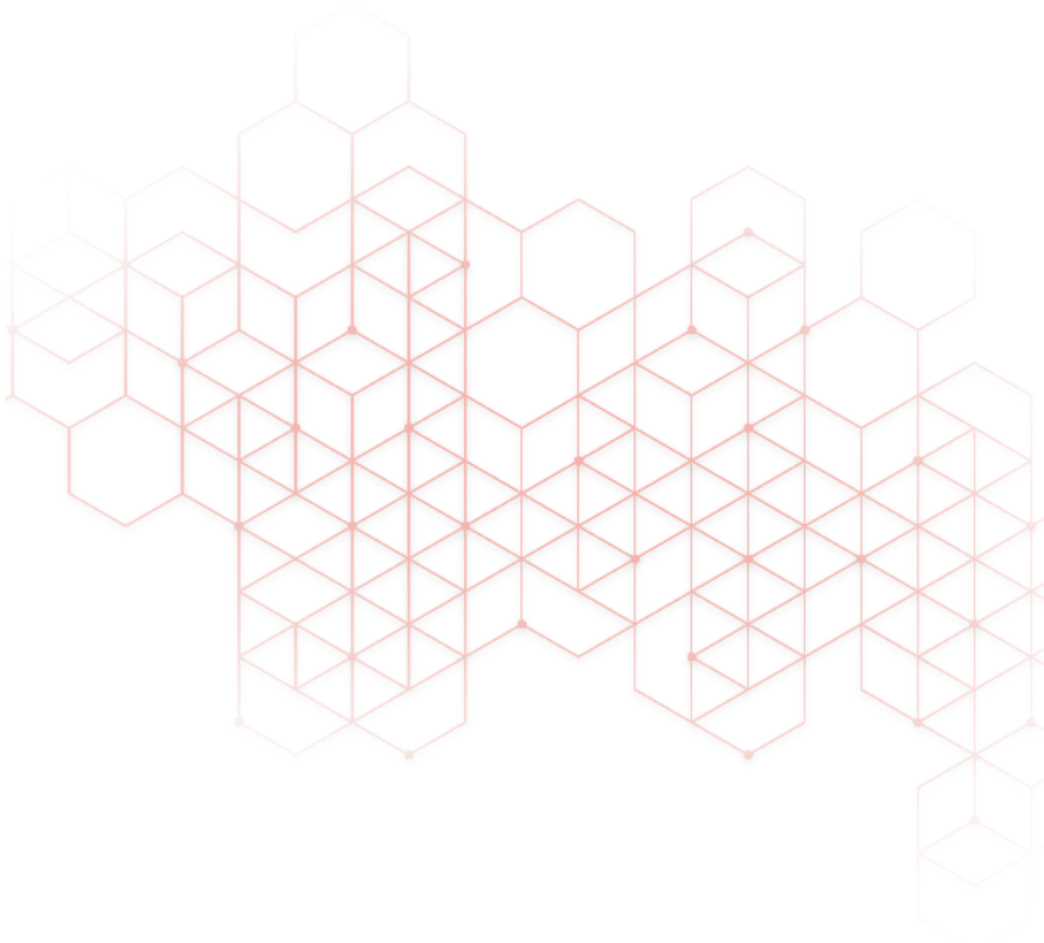

Credits

Disclaimer

This project has received funding from the European Union's Horizon Europe research and innovation programme under grant agreement No 101091456.

Technical references

Grant Agreement N°	101091456	Acronym	HyInHeat
Full Title	D3.4 - Report on H_2 fuel gas characteristics and flow measurement		
Work Package (WP)	WP3		
Authors	Elsa Busson, Carolin Lohrberg, Martin Oberländer, Lukas Sankowski		
Leading organisation	RWTH Aachen University		
Date of publication	17.12.2024		
Contributors	RWTH-IOB, SIEN		
Document Type	R – Document, report		
Document Title	Report on H_2 fuel gas characteristics and flow measurement		
Dissemination Level	Public		

Document history

Version	Date	Partner	Author
1	14.11.2024	RWTH-IOB	Busson, Sankowski
2	09.12.2024	RWTH-IOB, SIEN	Busson, Sankowski, Lohrberg, Oberländer
Final	16.12.2024	RWTH-IOB, SIEN	Busson, Sankowski, Lohrberg, Oberländer

Content

Tables & Figures

List of abbreviations

Abbreviations	Explanation
AFM	Area Flow Meter
BCU	Burner Control Unit
CC	Constant Current
CLD	Chemiluminescence Detector
CT	Constant Temperature
CV	Constant Voltage
EN	European Norm
Eq.	Equation
IEC	International Electrotechnical Commission
ISO	International Organization for Standardization
MFC	Mass Flow Controller
MFM	Mass Flow Meter
NCV	Net Calorific Value
NDIR	Non-Dispersive Infrared Sensor
NO_x	Nitrogen Oxides
P&I	Piping and Instrumentation Diagram
PEM	Proton Exchange Membrane
SOEC	Solid Oxide Electrolyzer Cell
SOS	Speed of Sound
TCD	Thermal Conductivity Sensor
USM	Ultrasonic Flow Meter
UV	Ultraviolet

Executive summary

This deliverable presents the findings from Task 3.5 of Work Package 3 (WP3), which focuses on assessing the impact of hydrogen (H_2) impurities (up to 2 vol%) on the accuracy of calibrated flow measurement technologies. Contamination of hydrogen with impurities can significantly alter its density and Wobbe index, thereby affecting the detection and regulation of fuel gas flows. In addition, this deliverable presents a methodology for estimating hydrogen purity using Ultrasonic Flow Meters.

Section 1 presents hydrogen impurities and relevant purity standards. Additionally, the theoretical effect of impurities on fuel and combustion characteristics are discussed.

Section 2 provides theoretical background information on the investigated flow measurement devices and the calculation of measurement uncertainties.

Section 3 details the investigations conducted by RWTH-IOB into the performance of three calibrated flow meters when hydrogen is mixed with various impurities:

- Mass Flow Meter (MFM)
- Area Flow Meter (AFM)
- Differential Pressure Meter with Orifice Plate

The impurities investigated include Methane (CH_4), Oxygen (O_2), Nitrogen (N_2), Carbon Monoxide (CO), Carbon Dioxide (CO_2) and Water (H_2O).

The key results are as follow:

- The MFM exhibits the highest accuracy among the devices tested, with deviation below 2.5% from expected flow rates across all data points.
- The AFM and Orifice Plate show significantly higher deviations up to 16% and 20% respectively, that correlate with the increasing density of the hydrogen-impurity mixtures.
- Deviations from the AFM and Orifice Plate can be corrected using a factor that accounts for changes in mixture density.

The section also highlights how these impurities influence pollutant emissions (NO_x and CO) and off-gas composition during combustion:

- Adding 2 vol% O_2 results in 32-37% increase in NO_x emissions, while introducing 2 vol% CH_4 leads to a decrease in NO_x emissions by 13-15%.
- The impurities caused notable changes in oxygen content within the off-gas.
- Impurities containing carbon (CH_4, CO, CO_2) lead to an increase in CO and CO_2 in the off-gas.

Section 4 presents two algorithms developed by SIEN for estimating the H_2 purity in ultrasonic flow meters based on measurement of speed of sound, as well as temperature and pressure. The uncertainty of the algorithms was determined with numerical simulations to be between 0.03 mol% and 0.09 mol% depending on the impurity gas. The algorithms were experimentally tested at SIEN facilities using a prototype ultrasonic flow meter for hydrogen. Nitrogen and Methane were used as impurity gases. Both algorithms were found to work as intended and the results of the measurements are in excellent agreement with the numerical simulations.

1. Introduction

The objective of Work Package 3 (WP3) is to provide documentation for the design of safe and efficient infrastructures for hydrogen and oxygen supply systems. Within this framework, Task 3.5 focuses on the influence of contamination of hydrogen with other species. Impurities can be introduced in hydrogen during production, storage or transportation. Given hydrogen's low density, even trace amounts of these impurities can significantly influence the density and Wobbe index of the resulting gas mixture, posing challenges for its use as a fuel in industrial applications. These changes can disrupt measurement systems used to measure and regulate fuel gas flows. This report aims to provide insights into the impact of impurities in hydrogen on calibrated flow measurement technologies.

To this end, RWTH-IOB investigates the performance of three calibrated flow meters – Mass Flow Meter (MFM), Area Flow Meter (AFM) and an orifice plate – in response to various hydrogen impurities. Additionally, the impact of the impurities on burner operation and off-gas composition is also examined. For this purpose, a semi-industrial test rig was installed at RWTH-IOB. The test rig consists of a gas mixing unit, the three flow meters and an industrial burner, which is installed within a furnace chamber.

Furthermore, SIEN investigates and enhances the functionality of a state-of-the-art ultrasonic flow meter by adding appropriate evaluation algorithms to estimate H_2 purity. This would be a significant advantage when using H_2 as a fuel, as even small concentrations of impurities impact the speed of sound in hydrogen and can be immediately detected along with the ultrasonic flow measurement.

1.1. Hydrogen production and impurities

Hydrogen can be produced by different production technologies [24], which are based on the use of fossil fuels, biomass or water:

- Fossil fuels
  - Steam reforming of hydrocarbons
  - Thermal cracking of hydrocarbons
  - Partial oxidation of heavy fractions
  - Coal gasification
- Biomass
  - Burning
  - Fermenting
  - Pyrolysis
  - Gasification and liquefaction
  - Biological production
- Water
  - Electrolysis (alkaline, PEM, SOEC)
  - Photolysis
  - Thermochemical processes
  - Thermolysis

All of these technologies have in common that the produced hydrogen contains impurities.

EN 17124 [8] provides an overview of impurities that can arise from different production technologies. These impurities are summarized in Table 1 for steam reforming, alkaline and PEM electerolysis as production technologies. In the standard, these impurities are categorized according to specific limits. However, it is important to note that EN 17124 [8] specifically defines quality specifications for hydrogen in fuel cell applications for vehicles. Therefore, the specific limits are not discussed here; only the types of impurities (species) are listed

Table 1: Simplified overview of impurities from different hydrogen production processes [8]

Production technology	Impurities
Steam reforming	N_2, Ar, CH_4, CO, (O_2, CO_2, H_2O, He, TS, NH_3THC (exc. CH_4), HCOOH, halogens)
Alkaline electrolysis	O_2, H_2O, CO_2, (N_2, Ar, CO, CH_4, He, TS, NH_3, THC, HCHO, HCOOH, halogens)
PEM electrolysis	O_2, H_2O, CO_2, (N_2, Ar, CO, CH_4, He, TS, NH_3, THC, HCHO, HCOOH, halogens)

1.2. Standards and Reports on Hydrogen Purity

The minimum quality characteristics of hydrogen fuel are specified in the international standard ISO 14687 [28]. According to the standard, hydrogen fuel can be classified into different groups, based on its application:

- Type I (grades A, B, C, D, E): Gaseous hydrogen and hydrogen-based fuel
- Type II (grades C, D): liquid hydrogen
- Type III: slush hydrogen

The standard defines the allowable impurities for different applications. For industrial applications and specifically thermoprocessing plants, no grade is specified in ISO 14687 [28]. However, different national standards and rules, e.g. [23], indicate the specifications of grade A. In ISO 14687 [28], grade A of hydrogen fuel is defined as gaseous hydrogen for "internal combustion engines for transportation, residential/commercial combustion appliances (e.g. boilers, cookers and similar applications)" with a minimum mole fraction of 98.0 mol%. Table 2 shows the defined impurity limit definitions for grade A.

*Table 2: Impurity limit definitions for grade A hydrogen acc. to [28]; *combined H_2O, O_2, N_2 and Ar: max. mole fraction of 1.9 mol%*

Species	Limit (maximum content)
Total gases	20,000 µmol/mol
Water (H_2O)	non-condensing at all conditions*
Total hydrocarbon	100 µmol/mol
Oxygen (O_2)	*
Argon (Ar)	*
Nitrogen (N_2)	*
Carbon monoxide (CO)	1 µmol/mol
Sulphur (S)	2 µmol/mol

1.3. Effect of impurities on hydrogen fuel gas properties

In the following investigations, the species O_2, CO_2, CO, CH_4, N_2 and H_2O are considered as impurities with a maximum concentration of 2 vol% in hydrogen. This value was chosen in accordance with the definition of grade A hydrogen, which requires a minimum mole fraction of 98.0 mol%, corresponding to 98 vol%, assuming ideal gas behaviour. The impurities were chosen based on the impurities listed in Table 1. The properties such as molar mass, density, heat capacity, net calorific value and minimum air requirement for the combustion of those species are given in Table 3.

Table 3: Properties of pure hydrogen and pure impurities

Properties	Unit	H_2	CH_4	O_2	N_2	CO	CO_2	H_2O (g)
Molar mass	g/mol	2.02	16.04	32.00	28.01	28.01	44.01	18.02
Density	kg/m³	0.09	0.72	1.43	1.25	1.25	1.96	0.80
Net calorific value	kWh/m³	3.00	9.97	0	0	3.51	0	0
Min. air requirement	m^3_{air}/m^3	2.38	9.52	-4.76	0	2.38	0	0
Spec. heat capacity (vol.)	kJ/Nm³K	1.29	1.75	1.31	1.30	1.30	1.60	1.49

According to Table 3, all the impurities have significantly higher molar masses and densities than that of pure hydrogen. Methane (CH_4), the impurity with the lowest density, is about 8 times that of hydrogen. Carbon dioxide (CO_2) is the impurity with the highest density, about 22 times that of hydrogen. It is also interesting to note that some impurities such as methane (CH_4) and carbon monoxide (CO) are combustible, whereas oxygen (O_2), nitrogen (N_2), carbon dioxide (CO_2) and water vapour (H_2O) are not. The net calorific value (NCV) of CO is 3.51 kWh/m³, about 17% higher than that of hydrogen, and CH_4 is 9.97 kWh/m³, about 3.3 times that of hydrogen. When considering the minimum air requirement, both H_2 and CO require about 2.38 m^3_{air}/m^3_{fuel}, while the minimum air requirement for CH_4 is about 4 times higher at 9.52 m^3_{air}/m^3_{fuel}. On the contrary, O_2 reduces the minimum air requirement by 4.76 m^3_{air}/m^3_{fuel} when present in a combustible mixture. The volumetric heat capacity of the impurities shows slight variations compared to that of pure hydrogen. Species such as N_2, O_2 and CO have similar volumetric heat capacities to hydrogen, around 1.30 kJ/Nm³K. Other species such as H_2O (g) and CO_2 have higher heat capacities, with CH_4 having the highest at 1.75 kJ/Nm³K.

To illustrate the theoretical impact of different impurities in hydrogen, the relative change in various properties and combustion characteristics of hydrogen/impurities mixtures compared to pure hydrogen are shown in Table 4 and Figure 1. Hydrogen purity is assumed to be 98 vol% and the impurity content to be 2 vol%.

Table 4: Change in properties and combustion characteristics of hydrogen and its mixtures with impurities

Properties	100 vol% H_2	98 vol% H_2 +					
		2 vol% CH_4	2 vol% O_2	2 vol% N_2	2 vol% CO	2 vol% CO_2	2 vol% H_2O
Molar mass	2.02 g/mol	+13.9%	+29.8%	+25.8%	+25.8%	+41.7%	+15.9%
Density	0.09 kg/m³	+13.9%	+29.8%	+25.8%	+25.8%	+41.7%	+15.9%
Net calorific value	3.00 kWh/m³	+4.7%	-2.0%	-2.0%	+0.3%	-2.0%	-2.0%
Lower wobbe index	11.34 kWh/m³	-2.0%	-14.0%	-12.6%	-10.5%	-17.7%	-9.0%
Min. air requirement	2.38 m^3_{air}/m^3	+6.0%	-6.0%	-2.0%	±0.0%	-2.0%	-2.0%
Spec. min. off-gas vol. (dry)	1,88 m^3_{og}/m^3	+7.1%	-6.0%	-0.9%	+1.1%	-0.9%	-2.0%
Spec. min. off-gas vol. (moist)	2.88 m^3_{og}/m^3	+5.3%	-4.6%	-1.3%	±0.0%	-1.3%	-1.3%
Spec. heat capacity (vol.)	1.288 kJ/Nm³K	+0.72%	+0.03%	+0.02%	+0.02%	+0.49%	+0.32%
Ad. Flame Temperature (T_{Air} = 25°C, λ = 1.13)	2051 °C	-0.6%	+2.0%	-0.5%	+0.1%	-0.7%	-0.6%

The presence of impurities in hydrogen significantly affects the density of the resulting mixture. Impurities with higher densities, such as CO_2, O_2, and N_2, cause significant increases in density of 41.7%, 29.8%, and 25.8%, respectively. These same impurities also have a substantial effect on the Wobbe index, with CO_2

reducing it by up to 17.7%. In contrast, CH_4, the impurity with the lowest density, only causes a reduction in the Wobbe Index of 2%. Overall, all mixtures containing impurities show a lower Wobbe Index compared to pure hydrogen. Regarding the Net Calorific Value (NCV), only combustible impurities, such as CH_4 and CO, increase this parameter. CH_4 contributes to a 4.7% rise in NCV, while CO results in an increase of 0.3%. Non-combustible impurities, on the other hand, uniformly reduce the NCV by approximately 2%. It is important to note, that this change in NCV will affect the resulting power output of the system. Impurities such as O_2, N_2, CO_2 and H_2O will reduce the power by 2% and CH_4 will increase it by almost 5% if the flow is not adjusted. A similar trend to that observed for the NCV is observed for the minimum air requirement. CH_4 increases the air requirement by 6%, while CO has no effect. This is due to the fact that H_2 and CO as species have the same oxygen demand and the reduction in hydrogen by 2 vol% is compensated by the 2 vol% CO. Oxygen as an impurity reduces the air requirement by 6%, and other non-combustible impurities decrease it by about 2%.

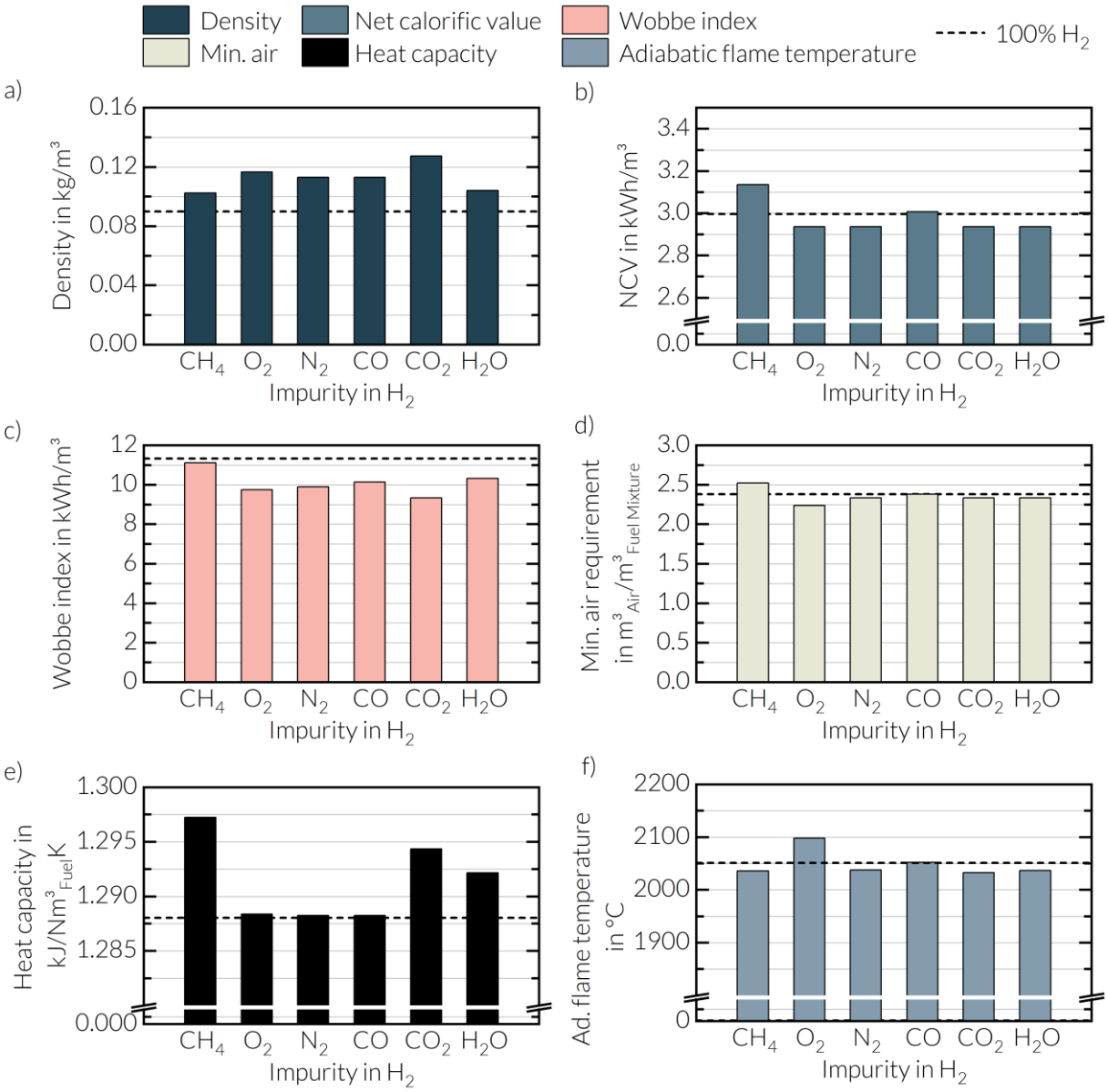

Figure 1: Properties and combustion characteristics of H_2 and its mixtures with 2 vol% impurities: a) density, b) net calorific value, c) Wobbe index, d) minimum air requirement, e) heat capacity and f) adiabatic flame temperature

The specific off-gas volume also changes depending on the type of impurity. Combustible impurities increase the off-gas volume, whereas O_2 decreases it due to its effect on air requirements, resulting in reductions of 6% for dry off-gas and 4.6% for moist off-gas. Other impurities lead to decreases in off-gas volume of about 1–2% for both dry and moist conditions. The change in volumetric heat capacity of the gas mixture is minimal,

with an increase ranging from 0.02% to 0.72%. Among the species studied, O_2, N_2 and CO have negligible impacts, contributing increases of less than 0.04%. CH_4, on the other hand, has the most significant effect, causing an increase of up to 0.72%. Lastly, the adiabatic flame temperature of the gas mixture also varies with the addition of impurities. O_2 as an impurity has the most significant impact, raising the adiabatic flame temperature from 2051 °C for pure hydrogen to 2098 °C. CO has an almost negligible effect. However, impurities such as N_2, CH_4 and H_2O and CO_2 cause a reduction of the adiabatic flame temperature to 2038 °C, 2036 °C, 2037 °C and 2034 °C, respectively.

2. Theoretical background

2.1. Flow measurement

For industrial flow measurement in closed pipelines, different measurement methods are available and commercialized, Figure 2. The measurement methods can be in divided into volumetric and mass flow meters. Volumetric flow meters include differential pressure meters, variable area, electromagnetic and ultrasonic flow meters. Mass flow meters include Coriolis and thermal mass meters. Throughout this work, only the methods applicable to the flow measurement of hydrogen within the experimental test rigs are described in more detail (framed).

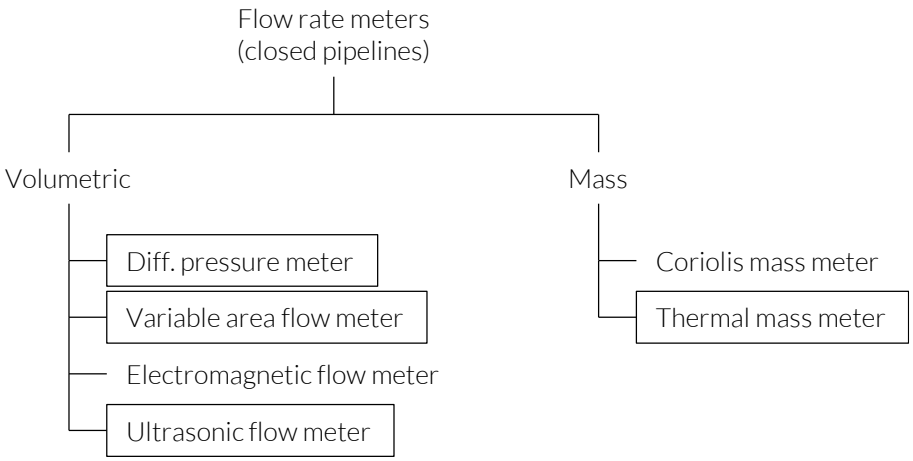

Figure 2: Overview of different measuring methods of flow rate meters in closed pipelines acc. to [1]

2.1.1. Differential pressure meter with orifice plate

Differential pressure meters are widely used flow measurement devices that determine the flow rate of a fluid by measuring the pressure difference across a restriction section in the pipeline. These are one of the most common technique for measuring flow rates. The volume flow measurement by differential pressure meters is described for different types of meters in the standard series EN ISO 5167.

According to Bernoulli's principle, a constriction in the pipeline leads to an increase in the velocity of the fluid, causing a pressure drop Δp across the constriction. Pressure and flow rate are therefore closely related. Differential pressure meters use this principle to determine the flow rate by measuring the pressure drop across a defined constriction. This measurement principle requires a first device to create the pressure drop and a second device to measure the resulting differential pressure. Pressure transducers are generally used to measure the differential pressure. There are several types of devices used to create the pressure drop, such as orifice plates, venturi nozzles, gate or target meters. In the following, only the principle of operation of orifice plates will be described. The design and volume flow measurement of orifice plates are defined in EN ISO 5167-2 [10].

The design principle of orifice plates is shown in Figure 3. These consist of a circular, and thin steel plate with a concentric circular orifice. This orifice is smaller in diameter than the pipeline in which the plate is installed [3]. The plate is typically clamped between two flanges in the pipeline. Pressure tappings on either side of the orifice plate are used to measure the differential pressure at the orifice. Figure 3 shows the design principles of an orifice plate with corner tappings. In this case, the pressure tappings are carried out as single tappings or annular slots. [19]

Orifice plates are best suited for measuring constant flow rates in medium and large pipes [3]. They have the advantage of being simple to use, available in a wide range of sizes, with no moving parts, long-term reliability and have comparatively low operating and acquisition costs. As a result, they represent almost 50% of the volume flow meters used in the industry [34]. However, they have the disadvantage of significant and irrecoverable pressure losses and have poor turndown ratios [19].

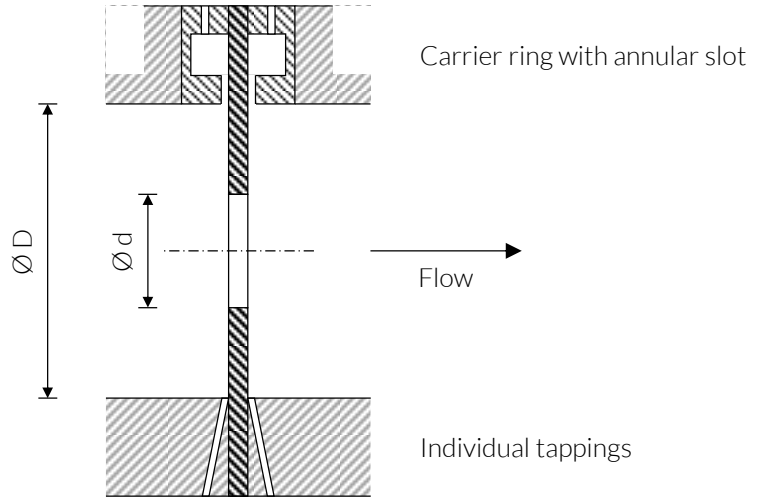

Figure 3: Orifice plate with corner tapping design as carrier ring with annular slot and individual tappings acc. to [10]

The calculation methods for the volume flow q_v and the mass flow q_m measured with orifice plates is defined in EN ISO 5167-2 [10].

The mass flow q_m and volume flow q_v are defined in Eq. (2.1) as:

$$q_m = q_v \cdot \rho = \frac{C}{\sqrt{1-\beta^4}} \cdot \varepsilon \cdot \frac{\pi}{4} \cdot d^2 \cdot \sqrt{2 \cdot \Delta p \cdot \rho_1} \tag{2.1}$$

where

C	Discharge coefficient
β	Diameter ratio; $\beta = d/D$
d	Inner diameter of orifice plate
ε	Expansion factor
Δp	Differential pressure
ρ_1	Density of the fluid at operating temperature (before the orifice plate)
ρ	Density of the fluid at the temperature and pressure for which the volume is stated

The discharge coefficient C is calculated by the Reader-Harris/Gallagher equation (Eq. (2.2)) in its modified form for orifice plates with corner tappings. It is dependent on the Reynolds number Re_D, which is itself dependent on the mass flow q_m. Therefore, it has to be obtained by iteration [10]. EN ISO 5167-1 [9] provides an overview of an iterative computation scheme.

$$C = 0.5961 + 0.0261 \cdot \beta^2 - 0.216 \cdot \beta^8 + 0.000521 \cdot \left(\frac{10^6 \cdot \beta}{Re_D}\right)^{0.7} + \left(0.0188 + 0.0036 \cdot \left(\frac{19000 \cdot \beta}{Re_D}\right)^{0.8}\right) \cdot \beta^{3.5} \cdot \left(\frac{10^6}{Re_D}\right)^{0.3} + 0.011 \cdot (0.75 - \beta) \cdot \left(2.8 - \frac{D}{25.4}\right) \tag{2.2}$$

where

D	Pipe inside diameter

The definition of the Reynolds number Re_D is given in Eq. (2.3):

$$Re_D = \frac{4 \cdot q_m}{\pi \cdot \mu_1 \cdot D} \tag{2.3}$$

where

μ_1 Dynamic viscosity of the fluid (before the orifice plate)

The expansion factor ϵ is calculated by Eq. (2.4) and is defined as a coefficient used to consider the compressibility of the fluid [9].

$$\varepsilon = 1 - (0.351 + 0.256 \cdot \beta^4 + 0.93 \cdot \beta^8) \cdot \left[1 - \left(\frac{p_2}{p_1}\right)^{1/\kappa}\right] \tag{2.4}$$

where

p_1 Static pressure (before the orifice plate)

p_2 Static pressure (behind the orifice plate); $p_2 = p_1 - \Delta p$

κ Isentropic exponent (varies for gas type, temperature and pressure)

The mass density ρ is calculated by Eq. (2.5) from the static pressure p_1, the temperature T, the gas molecular mass M, the compressibility Z and the gas constant R.

$$\rho = \frac{p_1 M}{ZRT} \tag{2.5}$$

2.1.2. Variable area flow meter

Variable area flow meters, commonly known as rotameters, are a simple and inexpensive method to measure flow rates. The measurement of the volume flow by variable area flow meters is based on the upward flow of a fluid through a vertical conical and transparent tube. The tube has the characteristics that its diameter increases in upward direction. The gas enters the flow meter through the bottom and exits through the top of the tube. Inside the tube, a float is lifted until equilibrium of the gravity force F_G, the buoyant force F_A and the flow resistance force F_S is reached. The flow rate can then be read on a graduated scale which is printed in the wall tube. With increasing flow rate, the float goes up to a larger tube diameter until it reaches equilibrium again. Figure 4 shows the measurement principle and the different forces. In this case, the float is carried out as a ball. However, a wide range of float types are also available. [2]

Variable area flow meters are often used for flow control, because of it's simplicity of operation and the position of the float inside the tube intuitively shows the flow rate, i.e. the higher the float the higher the flow rate. However, it must be installed vertically. The accuracy of rotameters can vary from ±5% for the cheapest devices to ±0.5% for more expensive versions [33]. However, the measurement can be affected by change in temperature and density of the fluid [2].

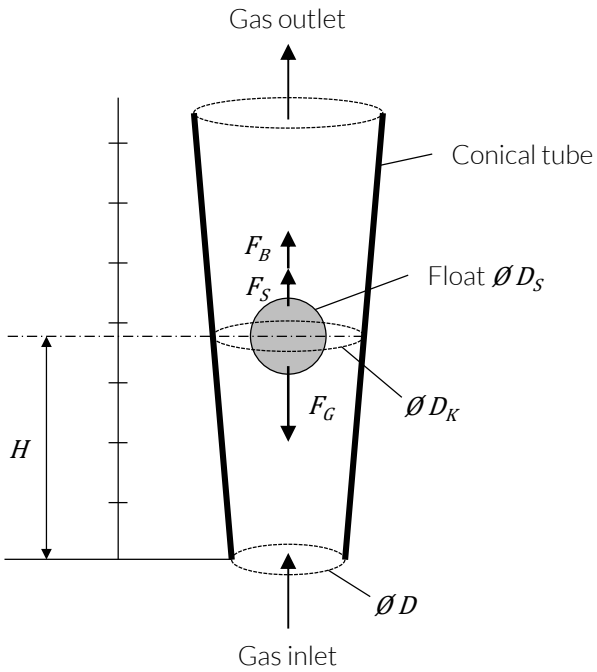

Figure 4: Principle of variable area flow meter acc. to [41; 1]

At the float, the gravitational force F_G, the buoyancy force F_A and the flow resistance force F_S form an equilibrium at the float position H, Eqs. (2.6) and (2.7). [42]

$$F_G = F_A + F_S \tag{2.6}$$

$$V_S \cdot \rho_S \cdot g = V_S \cdot \rho_{fl} \cdot g + c_w \cdot A_S \cdot \frac{\rho_m \cdot v^2}{2} \tag{2.7}$$

where

V_S	Volume of the float
ρ_S	Density of the float
g	Gravitational acceleration
ρ_{fl}	Density of the fluid
c_w	Resistance coefficient
A_S	Cross-sectional area of the float (at reading edge)
v	Flow velocity

The volume flow is given in Eq. (2.8), where D_K defines the inside diameter of the cone at the reading point and D_S the float diameter at the reading edge. [42]

$$q_v = v \cdot \frac{\pi}{4} \cdot (D_K^2 - D_S^2) \tag{2.8}$$

The general equation for calculation of the volume flow by variable area flow meter is given in Eq. (2.9).

$$q_v = \frac{\alpha}{\rho_{fl}} \cdot D_S \cdot \sqrt{g \cdot m_S \cdot \rho_{fl} \cdot \left(1 - \frac{\rho_{fl}}{\rho_S}\right)} \tag{2.9}$$

where

α Flow coefficient; $\alpha = \sqrt{1/c_w}$

m_S Mass of the float

2.1.3. Thermal mass meter

Thermal anemometry operates on the principle of electrically heating a sensor and measuring the cooling effect caused by the flow of a fluid over it. As the flow rate increases, the cooling increases. This relationship between flow rate and cooling allows for precise measurements of the flow velocity. Different heated elements can be used in thermal anemometer and result in different sensor types such as hot-wire, hot-film or hot-chip anemometers. Hot-wire anemometers have the advantage of having very small diameters. They are typically a few micrometres in diameter and a few millimetres in length. Hot-film anemometer have the advantage of being more robust, however their response to change is slower due to their larger thermal inertia. The use of hot-wire is however not well suited for industrial environments due to the fragility of the thin probe and its sensitiveness to contamination in rough environments. Furthermore, thermal anemometry is unsuited for low velocities since natural convection can lead to errors [37]. The operating principle of a hot film anemometer is shown in Figure 5.

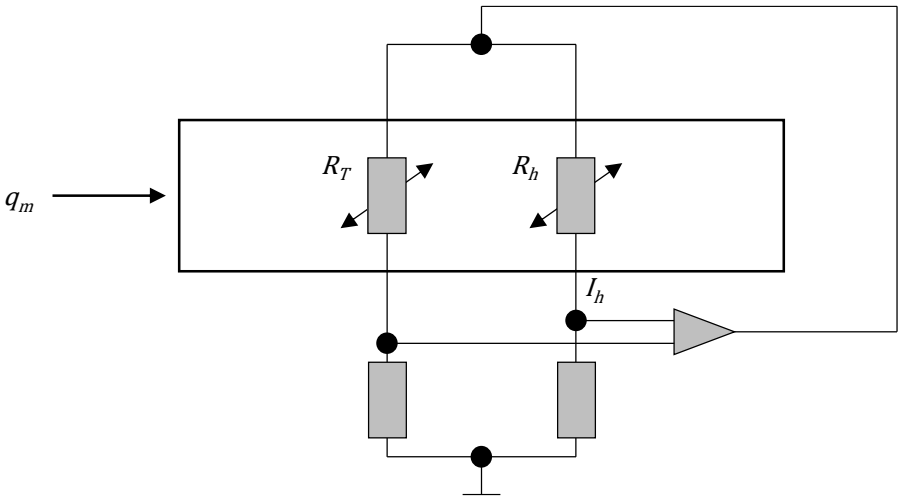

Figure 5: Principle of hot film anemometer acc. to [1]

In this case, two resistors are installed in an electrical bridge circuit and are in contact with the fluid flow. Resistor R_T takes the temperature of the fluid, whereas R_h is electrically heated to maintain a constant temperature above the fluid temperature. The fluid flow is cooling the second resistor R_h. The electrical power $\dot{Q}$ used to achieve the defined temperature is a measure for the mass flow q_m, Eq. (2.10). Here, c_p defines the specific heat capacity of the fluid at constant pressure and ΔT the temperature increase of the fluid. The mass flow is then calculated by Eq.(2.11).

$$\dot{Q} = q_m \cdot c_p \cdot \Delta T \tag{2.10}$$

$$q_m = \frac{I_h^2 \cdot R_h}{c_p \cdot \Delta T} \tag{2.11}$$

where

I_h Electric current

This control method is called constant temperature (CT) method. Other methods such as constant voltage (CV) and constant current (CC) are also possible. For hot-wire anemometers, CT is most commonly used.

2.1.4. Ultrasonic flow meter

Ultrasonic techniques are universally applicable for the measurement of both conductive and non-conductive liquids, as well as gases. Predominantly utilizing time-of-flight methods, an ultrasonic wave is continuously generated and propagated through the flowing medium between the transmission and reception points. The deformation of the sound field caused by the flow results in a variation in transit time, which is correlated to the volumetric flow rate using physical models. The operational principles of transit time ultrasonic methods for flow measurement confer specific functional characteristics that are critical for numerous applications:

- Applicable to all liquids and gases,
- Long-term stability with a wear-free measuring principle devoid of moving parts,
- High temporal resolution (transit times generally <1 ms),
- Direction detection (positive and negative transit time differences),
- Provision of additional information regarding material properties or composition through simultaneous measurement of the sound velocity of the flowing medium [38].

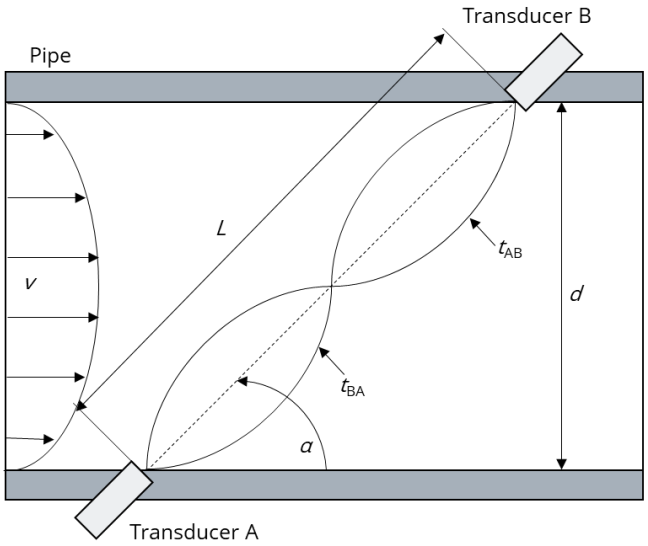

Figure 6: Basic structure of a transit time difference measurement according to [38]

The calculation of the fluid velocity v in pipes is based on the measurement of signal transit times Ultrasonic transducers, which can function as both transmitters and receivers of sound signals, are used to determine signal propagation times in both directions, as shown in Figure 6. Due to the acoustic entrainment effect [21], the sound signal travels faster in the direction of the flow than against it. The fluid velocity in the pipe can be derived from the absolute and differential transit times of both measurement directions. This method is commonly referred to in the literature as the "transit time difference method." Assuming an invariable pipe geometry described by the measuring path length L and the inclination angle α, it is therefore possible to determine the flow velocity v_{path} averaged over the measuring path by measuring transit times t_{AB} and t_{BA} in the forward and reverse directions. By distributing additional measuring paths across the pipe cross-section, a significantly more precise determination of the prevailing flow velocity v_{m} can be achieved.

$$t_{AB} = \frac{L}{(c_{fluid} + v \cdot \cos\alpha)} \tag{2.12}$$

$$t_{BA} = \frac{L}{(c_{fluid} - v \cdot \cos\alpha)} \tag{2.13}$$

$$v_{path} = \frac{L}{2\cos\alpha}\left(\frac{1}{t_{AB}} - \frac{1}{t_{BA}}\right) \tag{2.14}$$

$$v_m = \frac{1}{N}\sum_{i=1}^{N} v_{pathi} \tag{2.15}$$

The transit time difference method offers the advantage of being independent of the speed of sound of the fluid c_{fluid}.

2.2. Measurement uncertainty

When evaluating measurement data, it is important to express and consider the uncertainty in measurement. The ISO/IEC Guide 98-3 [27] provides principles for evaluating and reporting this measurement uncertainty, defining it as a "parameter, associated with the result of a measurement, that characterizes the dispersion of the values that could reasonably be attributed to the measurand". This uncertainty must account for all potential sources of error and their combined effects. In the following, the term *measurand* is defined as "a particular quantity subject to measurement" [27].

Generally, the measurand Y is not measured directly, but is instead calculated from other input quantities X_i through a function f.

$$Y = f(X_1, X_2, \dots, X_N) \tag{2.16}$$

These input quantities X_i may themselves be measurands and can also depend on other quantities. The measurement result is typically an approximation or an estimate of the measurand. To find an estimate y of the measurand Y, the corresponding input estimate x_i are used. The estimate y is defined as:

$$y = f(x_1, x_2, \dots, x_N) \tag{2.17}$$

Each input estimate x_1 is associated with a *standard uncertainty* $u(x_i)$. The estimated standard deviation of y, denoted as the *combined standard uncertainty* $u_c(y)$ is determined by the standard uncertainty $u(x_i)$ of each input estimate, which are expressed as standard deviations.

First, the standard uncertainty $u(x_i)$ of each estimate x_i must be determined. There are two different ways of assessing it: Type A and Type B evaluation, both of which rely on probability distributions. Type A evaluation involves statistical analysis of repeated measurements, whereas Type B evaluation is based on non-statistical methods, such as the manufacturer's specifications, previous data measurement or data provided in calibration certificates. [27]

For a type A evaluation, several independent measurements of the same quantity must be performed under the same conditions. Then, the arithmetic mean $\bar{x}$ of a series of n measurements is calculated. The formula is given in Eq. (2.18) by the sum of all observations q_i, divided by the number of observations n.

$$\bar{x_i} = \frac{1}{n} \cdot \sum_{i=1}^{n} q_i = \frac{q_1 + q_2 + \cdots + q_n}{n} \tag{2.18}$$

In order to quantify the spread of the data, the standard deviation of the measurement is calculated. The standard deviation s of a single observation q_i from the arithmetic mean $\bar{x}$ is defined in Eq. (2.19). It is used to show the variation from the averaged value.

$$s = \sqrt{\frac{\sum_{i=1}^{n}(q_i - \bar{x})^2}{n-1}} = \sqrt{\frac{n \cdot \sum_{i=1}^{n} q_i^2 - (\sum_{i=1}^{n} q_i)^2}{n \cdot (n-1)}} \tag{2.19}$$

In order to express the accuracy of the mean $\bar{x}$, u is calculated in Eq. (2.20) as the standard uncertainty of the mean $u(\bar{x_i})$.

$$u(\bar{x}_i) = \frac{s}{\sqrt{n}} = \sqrt{\frac{\sum_{i=1}^{n}(q_i - \bar{x}_i)^2}{n \cdot (n-1)}} \quad (2.20)$$

For type B evaluation, the uncertainty must be quantified by analysing each possible source of error. Relevant information, such as the manufacturer's specifications, reference data from standards, calibration reports, or prior measurements, can be used for this purpose. An appropriate probability distribution - such as uniform (rectangular), normal (Gaussian) or triangular - must then be assigned to each uncertainty based on the nature of the data.

The standard uncertainty can then be calculated according to Eq. (2.21).

$$u(x_i) = \frac{a}{k} \quad (2.21)$$

where a represents the half-width of the uncertainty range (e.g., $\pm a$) of x_i, obtained from the known information. The factor k depends on the selected probability distribution. Specifically, $k = \sqrt{3}$ for a uniform (rectangular) distribution, $k = 2$ for a normal (Gaussian) distribution and $k = \sqrt{6}$ for a triangular distribution.

After determining the standard uncertainty $u(x_i)$ of each input quantities, the *combined standard uncertainty* $u_c(y)$ of the measurement result y is calculated. It is defined as the positive square root of a sum of the variances of the quantities used in the measurement, each weighted by the sensitivity of the result to changes in those quantities. For uncorrelated input quantities, the combined standard uncertainty $u_c(y)$ for a measurement with independent variables is defined in Eq. (2.22).

$$u_c(y) = \sqrt{\sum_{i=1}^{N}\left(\frac{df}{dx_i}\right)^2 u^2(x_i)} \quad (2.22)$$

Here, $u(x_i)$ is a standard uncertainty gained from a type A or type B evaluation.

Additive and multiplicative relations between uncertainty variables result in special cases, where the combined standard uncertainty is given by Eq. (2.23) for additive and Eq. (2.24) for multiplicative relations.

$$y = x_1 \pm x_2 \pm \cdots \pm x_k \quad \rightarrow \quad u_c(y) = \sqrt{\sum_{i=1}^{k}(u_i)^2} \quad (2.23)$$

$$y = x_1 \cdot x_2 \cdot \ldots \cdot x_k \quad \rightarrow \quad \frac{u_c(y)}{\bar{x}_i} = \sqrt{\sum_{i=1}^{k}\left(\frac{u_i}{\bar{x}_i}\right)^2} \quad (2.24)$$

The *expanded uncertainty* U is defined as "an interval about the result of a measurement that may be expected to encompass a large fraction of the distribution of values that could reasonably be attributed to the measurand". It is determined by multiplying the combined standard uncertainty $u_c(y)$ by a coverage factor k, typically in the range 2 to 3, which reflects the confidence level of the interval. [27]

$$U = k \cdot u_c(y) \quad (2.25)$$

Finally, the result of the measurement y is expressed as:

$$Y = y \pm U \quad (2.26)$$

This equation indicates that the best estimate of the measurand value, Y, is y. The interval from $y - U$ to $y + U$ represents a range that is likely to include a significant portion of the values that could reasonably be attributed to Y.

3. Investigation of the effect of impurities on calibrated flow meters

3.1. Experimental setup

The experimental trials are carried out at a semi-industrial test rig in the IOB laboratory at RWTH Aachen, which is shown in Figure 7. It consists of a furnace chamber with off-gas duct, an industrial burner, a gas mixing unit, a flow measurement panel with different devices and a process control and measurement unit via PC.

From the bottom of the furnace, a Kromschröder BIC (65HB-300/335-(34)E) burner [14] is installed and is burning vertically into the furnace chamber. The burner has a nominal capacity of 50 kW and is equipped with standard ignition electrode and UV sensor for flame monitoring [18]. The valves at the burner fuel inlet are automatically opened and closed by a standard Burner Control Unit (BCU, type 400 by Kromschröder, [13]). Within the fuel inlet, the pressure is measured by a sensor of type A-10 by WIKA [43].

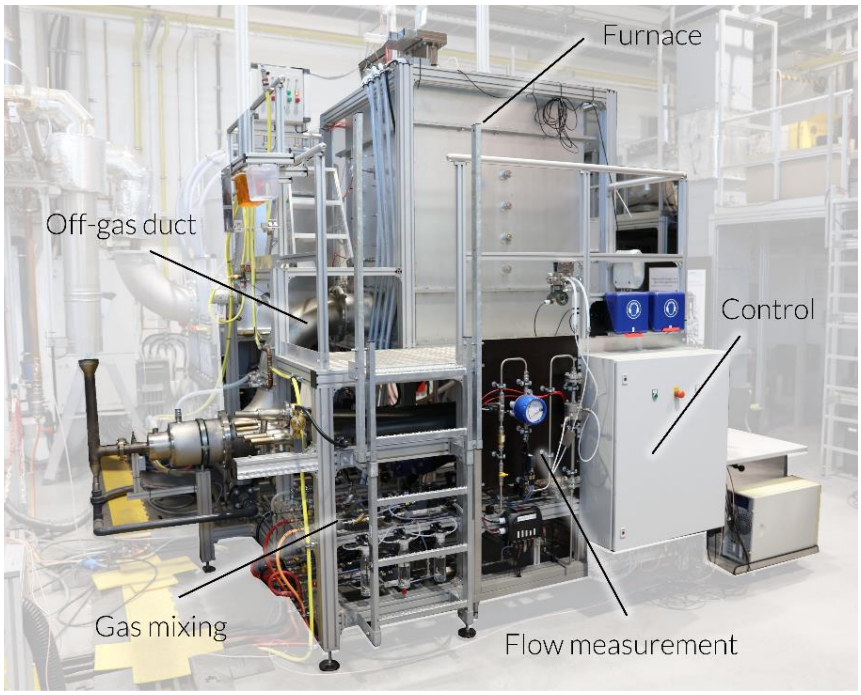

Figure 7: Overview of the semi-industrial experimental test rig at RWTH-IOB

The inner dimensions of the square furnace chamber are 650 x 650 mm and the inner height is 1000 mm. The furnace lining consists of insulation with a thickness of 300 mm. The inner layer is designed to withstand furnace temperatures of 1400 °C. Six equidistant thermocouples T_1 to T_6 (type N, class 1, [7]) are installed in the furnace wall to measure the temperature distribution along the furnace height. A double thermocouple $T_{Furnace}$ (type S, class 1, [7]) is used to monitor the furnace temperature. Four indirect air-cooling tubes are mounted on the top of the furnace to simulate a thermal load and control a constant furnace temperature. For visual access, two inspection windows are installed on two furnace walls. A 3D model of the furnace is shown in Figure 8.

The media supply of the test rig is shown in Figure 9 as a P&I diagram. An overview of the components is given in Table 7. Hydrogen (H_2 5.0 with a purity of >99.999 mol%) is supplied from a gas cylinder and the main flow is regulated by the Mass Flow Controller 7 (MFC). Several gas supply lines are installed to investigate different impurities of up to 2 vol% in hydrogen. The species CO, CO_2, N_2, O_2 and CH_4 are supplied by gas cylinders and their flows are controlled by MFCs 2 to 6. To mix H_2O into hydrogen, the H_2 flow is divided into two streams. The smaller flow (MFC 8) is passes through three water wash bottles to take up H_2O. The humidity sensor (MI 201) measures the dew point T_{DP} of the gas mixture in the range of -110 °C to 20 °C. The humidity y_{H_2O} of the gas mixture can then be calculated using Eq. (2.28). [40]

$$y_{H_2O} = \frac{E(T_{DP})}{p_{abs}} = \frac{1}{p_{abs}} \cdot 611.20\ Pa \cdot \exp\left(\frac{17.62 \cdot T_{DP}}{243.12 + T_{DP}}\right) \quad (2.27)$$

where

$E(T_{DP})$ Saturated vapour pressure

p_{abs} Absolute pressure

The hydrogen flows are manually adjusted until the desired H_2O admixture is achieved. The pressure and the temperature of the gas mixture are measured at PI 202 and TI 203 respectively.

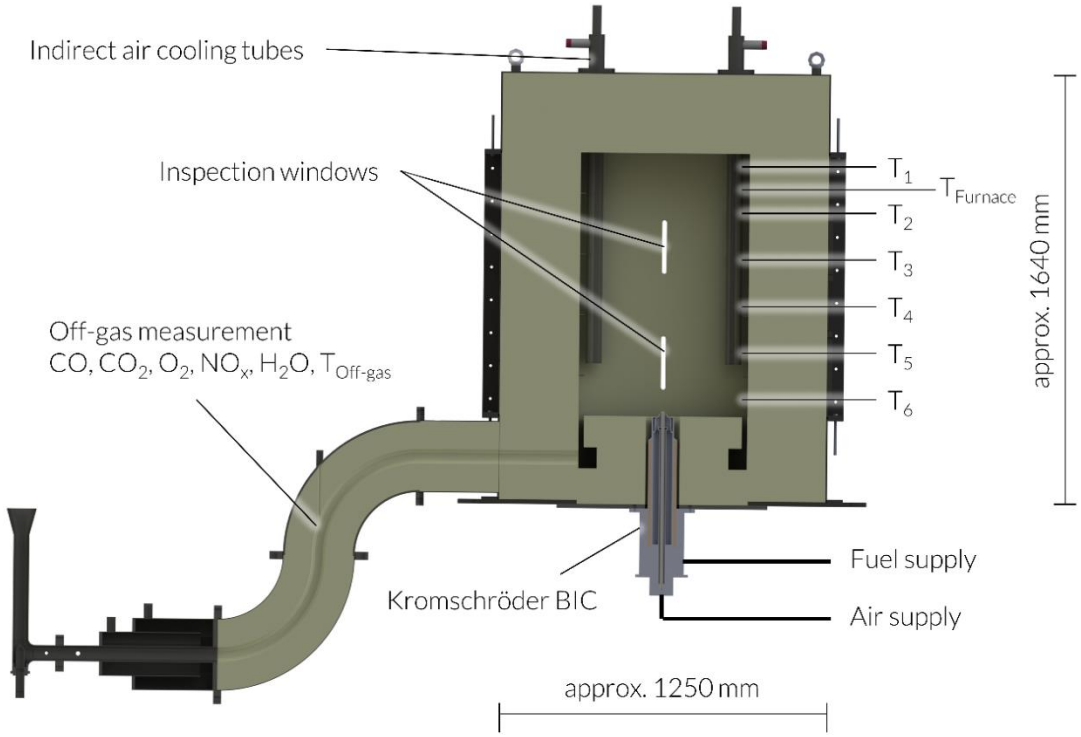

Figure 8: 3D model of experimental test rig at RWTH-IOB

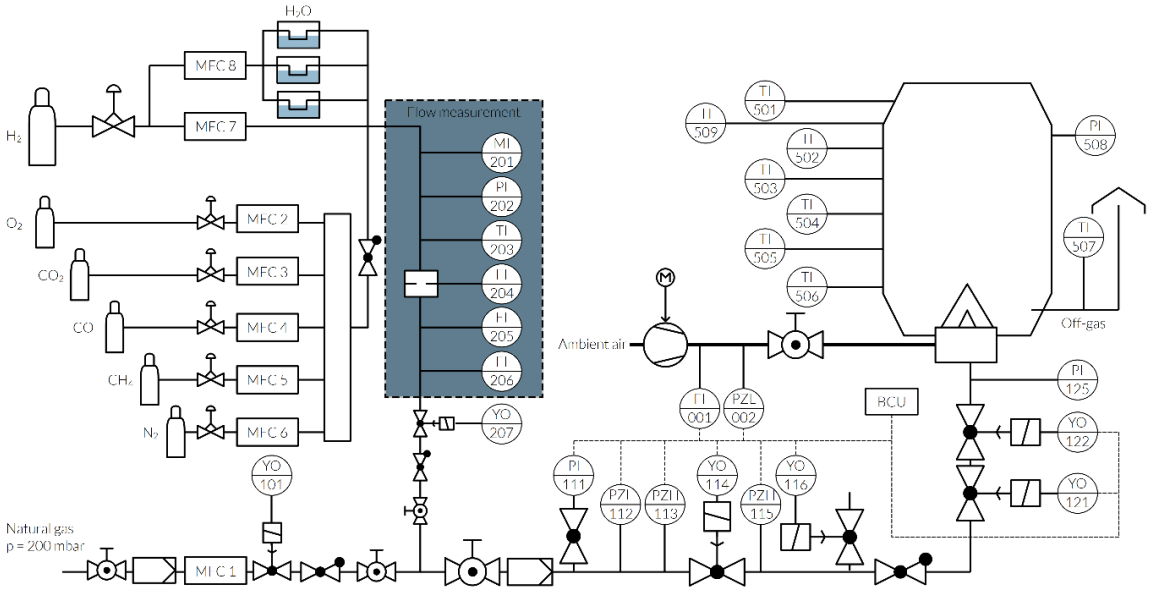

Figure 9: P&I diagram of experimental test rig at RWTH-IOB

The flow measurement is conducted by three different measurement devices in the following order:

- Corner-tapping orifice plate (type V16 by Dosch) with differential pressure transmitter (type P34 by halstrup-walcher [25]) at FI 204
- Thermal Mass Flow Meter (MFM, type 8742 by Bürkert [5]) at FI 205
- Variable Area Flow Meter (type H250 by Krohne [31]) at FI 206

An overview of the calibrated flow measurement devices is shown in Figure 10.

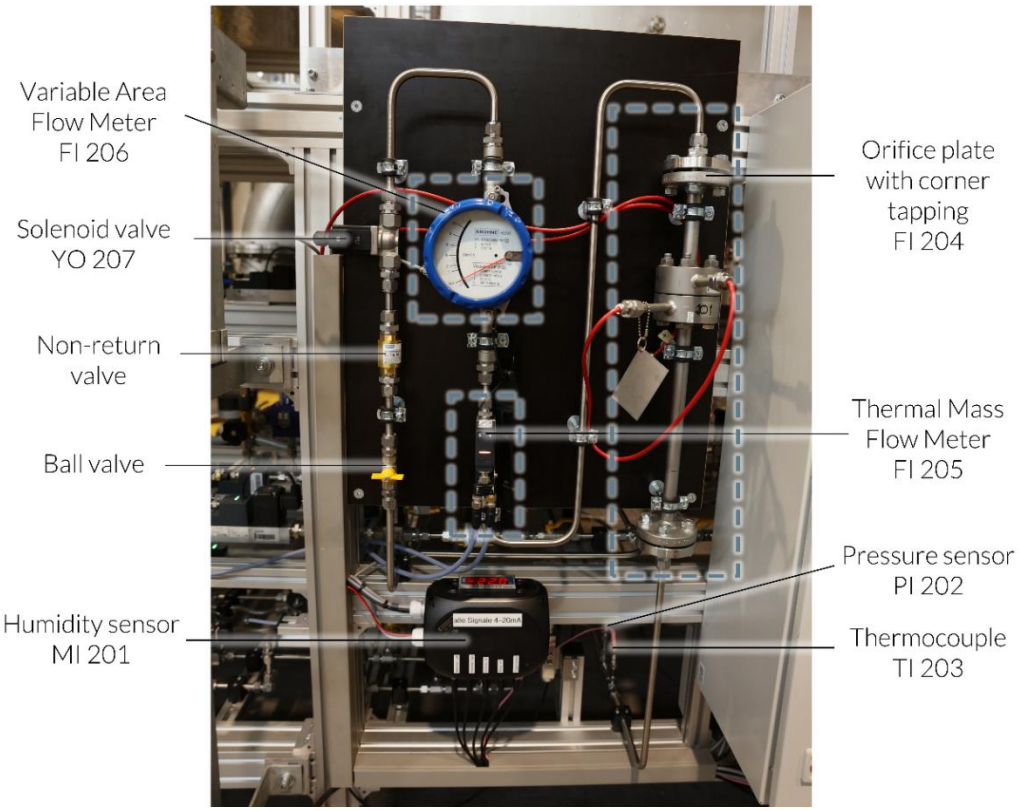

Figure 10: Overview of the calibrated flow measurement devices

The thermal mass flow meter and the area flow meter are designed for hydrogen flows up to 10 m^3/h. The specifications of the orifice plate are listed in Table 5.

Table 5: Specifications of the orifice plate (type V16 by Dosch)

Internal pipe diameter	Diameter of orifice	Diameter ratio	Isentropic exponent
D	d	β	κ
15.76 mm	4.29 mm	0.272	1.40

After passing through the flow measurement devices, the hydrogen mixture enters the gas safety train designed in compliance with ISO 13577-2 [29], before entering the burner. The gas safety train comprises the following components: a ball valve, a gas filter, a pressure gauge (PI 111), pressure switches for low (PZL 112) and high pressure (PZH 113 and 115), an automatic shut-off valve magnetic valve (YO 114), a solenoid valve for pressure relief (YO 116) and a second ball valve for manual close off of the gas train.

Additionally, a natural gas line is installed and natural gas is supplied by the grid by MFC 1. By activating either the hydrogen valve (YO 207) or the natural gas valve (YO 101), the burner can operate using either natural gas or the hydrogen/impurity mixture.

The combustion air is supplied to the burner by a side channel compressor (SCL K06-MS by FPZ) and controlled by a frequency converter. The volume flow is measured by a thermal measuring tube (FI 001) with an internal diameter of D_i = 41.8 mm.

The control and measurement system is implemented in a LabVIEW™ routine that is connected to the BCU to start and stop the burner.

The temperature (TI 507) and the off-gas composition are measured continuously in the off-gas duct. For the measurement of the off-gas composition, a small portion (approx. 60 l/h) of off-gas is extracted from an outlet port, dried and analysed. The analysis of the dry off-gas is performed with an X-Stream device from Emerson, which measures the species CO (non-dispersive infrared sensor, NDIR), CO_2 (NDIR), CH_4 (NDIR), H_2 (thermal conductivity sensor, TCD), and O_2 (paramagnetic sensor). NO_x emissions are measured in the dry off-gas using a chemiluminescence detector (CLD) analyser from Emerson. In addition, the water content in the off-gas is measured using a hygrometer from Bartec (Hygrophil). The specifications of the analysers are given in Table 6.

Table 6: Specifications of the off-gas analyser systems Emerson X-Stream, Emerson CLD and Hygrophil

Analyser	Emerson X-Stream					Emerson CLD	Bartec Hygrophil
Channel	1	2	3	4	5		
Species	CO	CO_2	CH_4	H_2	O_2	NO_x	H_2O
Measuring principle	NDIR	NDIR	NDIR	TCD	Paramag.	Chemilum.	Hygro-meter
Measuring range	0-5 vol%	0-17.5 vol%	0-5 vol%	0-25 vol%	0-25 vol%	0-500 ppm	2-100 vol%
Repeatability	< 1% (rel. to full scale)						
Resolution	0.01 vol%					0.1 ppm	0.1 vol%

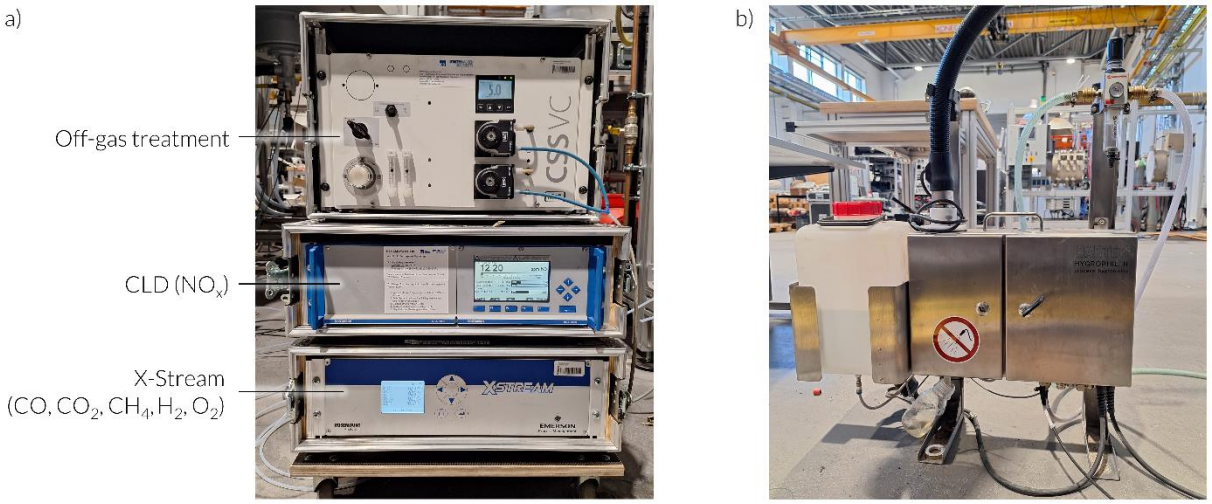

Figure 11: Off-gas analyser systems a) Emerson X-Stream, Emerson CLD and b) Hygrophil

Table 7: Overview of the P&I diagram for the test rig at RWTH-IOB

Medium/ position.	ID	Description	Manufacturer	Type
Combustion air	-	Side channel compressor	FPZ	K06 MS [20]
	FI 001	Thermal measuring tube	Höntzsch	TA-Di [26]
	PZL 002	Differential pressure switch	Kromschröder	DG [16]
Natural gas	YO 101	Diaphragm valve	Bürkert	0290 [6]
Gas safety train	PI 111	Pressure gauge	Kromschröder	KFM [15]
	PZL 112	Low pressure cut-off switch	Kromschröder	DG [16]
	PZH 113	High pressure protection	Kromschröder	DG [16]
	YO 114	Shut-off solenoid valve	Kromschröder	VAS [17]
	PZH 115	High pressure protection	Kromschröder	DG [16]
	YO 116	Pressure relief solenoid	Kromschröder	VAS [17]
	YO 121	Plunger valve	Bürkert	6027 [4]
	YO 122	Plunger valve	Bürkert	6027 [4]
	PI 125	Pressure sensor	WIKA	A-10 [43]
Flow measurement	MI 201	Humidity sensor	Michell	Easidew [35]
	PI 202	Pressure sensor	First Sensor	KTE
	TI 203	Thermocouple (type N, [7])	-	-
	FI 204	Orifice plate acc. to [30]	Dosch	V16
		Differential pressure sensor	halstrup-walcher	P34 [25]
	FI 205	Mass Flow Meter	Bürkert	8742 [5]
	FI 206	Variable Area Flow Meter	Krohne	H250 [31]
	YO 207	Diaphragm valve	Bürkert	0290 [6]
Furnace	TI 501	Thermocouple (type N, [7])	-	-
	TI 502	Thermocouple (type N, [7])	-	-
	TI 503	Thermocouple (type N, [7])	-	-
	TI 504	Thermocouple (type N, [7])	-	-
	TI 505	Thermocouple (type N, [7])	-	-
	TI 506	Triple thermoc. (type K, [7])	-	-
	TI 507	Thermocouple (type N, [7])	-	-
	PI 508	Pressure sensor	halstrup-walcher	P34 [25]

3.2. Experimental plan

At the beginning of every experimental trial, the furnace is heated with natural gas to a constant furnace temperature of $T_{Furnace}$ = 950 °C. The burner is then operated with hydrogen or hydrogen/impurity mixtures.

As outlined in section 1.2, a maximum impurity concentration of 2 vol% in hydrogen is assumed for industrial applications. The investigated impurities include Methane (CH_4), oxygen (O_2), nitrogen (N_2), carbon monoxide (CO), carbon dioxide (CO_2) and water (H_2O). Table 8 summarizes the experimental trials conducted.

In the baseline Case 0, the combustion of pure hydrogen is investigated. For all other cases, a single species is added to the hydrogen flow at concentrations up to 2 vol%. However, for H_2O, the admixture was limited to 1.0 vol%, as the gas flow was then saturated at the current process settings. To achieve a higher water admixture, either the pressure in the pipe must be reduced or the gas temperature needs to be increased to at least 33 °C, which was not feasible with the existing test rig.

Table 8: Investigated mixtures at RWTH-IOB

Species	Unit	Case 0	Case 1	Case 2	Case 3	Case 4	Case 5	Case 6
H_2	[vol%]	100.00	98.00	98.00	98.00	98.00	98.00	99.00
CH_4	[vol%]	0.00	2.00	0.00	0.00	0.00	0.00	0.00
O_2	[vol%]	0.00	0.00	2.00	0.00	0.00	0.00	0.00
N_2	[vol%]	0.00	0.00	0.00	2.00	0.00	0.00	0.00
CO	[vol%]	0.00	0.00	0.00	0.00	2.00	0.00	0.00
CO_2	[vol%]	0.00	0.00	0.00	0.00	0.00	2.00	0.00
H_2O	[vol%]	0.00	0.00	0.00	0.00	0.00	0.00	1.00

Three different output power levels (16 kW, 20 kW, and 24 kW) and their corresponding volume flows were investigated. In Case 0, the combustion air volume flows were adjusted to achieve an oxygen content of 3 vol% in the dry off-gas, corresponding to an air ratio of approximately $\boldsymbol{\lambda}$ = 1.13. For all subsequent cases, the combustion air flow was held constant.

Table 9 presents the calculated volume flows for each species and the combustion air. The gas flows were regulated using individual mass flow controllers (MFCs) and, in the case of H_2O admixture, verified through humidity measurements. To minimize random measurement errors, each test point was repeated three times.

Table 9: Volume flows for the different species for the experimental trials at RWTH-IOB

Power	Species	Unit	Case 0	Case 1	Case 2	Case 3	Case 4	Case 5	Case 6	$\dot{V}_{Air}$
16 kW	H_2	[m³/h]	5.34	5.23	5.23	5.23	5.23	5.23	5.23	15.10
	CH_4	[m³/h]	0.00	0.11	0.00	0.00	0.00	0.00	0.00	
	O_2	[m³/h]	0.00	0.00	0.11	0.00	0.00	0.00	0.00	
	N_2	[m³/h]	0.00	0.00	0.00	0.11	0.00	0.00	0.00	
	CO	[m³/h]	0.00	0.00	0.00	0.00	0.11	0.00	0.00	
	CO_2	[m³/h]	0.00	0.00	0.00	0.00	0.00	0.11	0.00	
	H_2O	[kg/h]	0.00	0.00	0.00	0.00	0.00	0.00	0.04	
20 kW	H_2	[m³/h]	6.67	6.54	6.54	6.54	6.54	6.54	6.54	18.38
	CH_4	[m³/h]	0.00	0.13	0.00	0.00	0.00	0.00	0.00	
	O_2	[m³/h]	0.00	0.00	0.13	0.00	0.00	0.00	0.00	
	N_2	[m³/h]	0.00	0.00	0.00	0.13	0.00	0.00	0.00	
	CO	[m³/h]	0.00	0.00	0.00	0.00	0.13	0.00	0.00	
	CO_2	[m³/h]	0.00	0.00	0.00	0.00	0.00	0.13	0.00	
	H_2O	[kg/h]	0.00	0.00	0.00	0.00	0.00	0.00	0.05	
24 kW	H_2	[m³/h]	8.01	7.85	7.85	7.85	7.85	7.85	7.85	21.65
	CH_4	[m³/h]	0.00	0.16	0.00	0.00	0.00	0.00	0.00	
	O_2	[m³/h]	0.00	0.00	0.16	0.00	0.00	0.00	0.00	
	N_2	[m³/h]	0.00	0.00	0.00	0.16	0.00	0.00	0.00	
	CO	[m³/h]	0.00	0.00	0.00	0.00	0.16	0.00	0.00	
	CO_2	[m³/h]	0.00	0.00	0.00	0.00	0.00	0.16	0.00	
	H_2O	[kg/h]	0.00	0.00	0.00	0.00	0.00	0.00	0.06	

3.3. Uncertainties of the measurements

The uncertainty in measured flow values arises from several sources. First, the gas mixture is mixed using multiple mass flow controllers, each with inherent uncertainty, introducing potential errors in the set volume flow. Second, each of the three volume flow measurement devices—MFM, AFM, and the orifice plate—has its own associated uncertainty. It is important to calculate and consider each of these uncertainties in order to evaluate the results of the experimental investigations.

The measurement uncertainty U of the MFM, MFCs and of the area flow meter are dependent on the maximum flow rate of the device $\dot{V}_{i,max}$ and the measured volume flow $\dot{V}_{i,measured}$. The specifications for the absolute measurement error of the MFM and MFCs are given in the data sheet [5] as:

$$U_{MFM} = 0.8\% \cdot \dot{V}_{MFM,measured} + 0.3\% \cdot \dot{V}_{MFM,max} \quad (2.28)$$

$$U_{MFC} = 0.8\% \cdot \dot{V}_{MFC,measured} + 0.3\% \cdot \dot{V}_{MFC,max} \quad (2.29)$$

For the area flow meter, the measurement uncertainty can be calculated as [31]:

$$U_{AFM} = 1.6\% \cdot \dot{V}_{AFM,measured} + 1.5\% \cdot \dot{V}_{AFM,max} \quad (2.30)$$

The maximum flow rates of the devices are listed for each device in Table 10.

Table 10: Maximum value of the MFCs, MFM and AFM

Device	Specie	Max. flow in m^3/h
MFC 2	O_2	0.40
MFC 3	CO_2	0.34
MFC 4	CO	0.17
MFC 5	CH_4	0.21
MFC 6	N_2	0.42
MFC 7	H_2	20.00
MFC 8	H_2	10.00
MFM	H_2	10.00
Area Flow	H_2	10.00

Determining the measurement uncertainty of orifice plates is more complex because of multiple sources of error. However, it's calculation is described in detail in EN ISO 5167-1 [9].

The mass flow at an orifice plate is calculated as described in chapter 2.1.1 and according to Eq. (2.1). It is therefore a function of different quantities such as the discharge coefficient C, the expansion number ε, the pipe and orifice plates dimension D and d, the differential pressure Δp and the density of the fluid ρ.

$$q_m = f(C, \varepsilon, D, d, \Delta p, \rho) \quad (2.31)$$

The relative standard uncertainty u'_{qm} of the mass flow q_m for orifice plates is given in Eq. (2.32) [9].

$$u'_{qm} = \sqrt{{u'_C}^2 + {u'_\varepsilon}^2 + \left(\frac{2\beta^4}{1-\beta^4}\right)^2 \cdot {u'_D}^2 + \left(\frac{2}{1-\beta^4}\right)^2 \cdot {u'_d}^2 + \left(\frac{1}{2}\right)^2 \cdot {u'_{\Delta p}}^2 + \left(\frac{1}{2}\right)^2 \cdot {u'_\rho}^2} \quad (2.32)$$

First, the relative standard uncertainty u' of each quantity must be calculated. In ISO 5261-1, the equations for the calculation of the uncertainties of each quantity are given as the relative expanded uncertainty U'_i with a confidence level of approximately 95%. The relative standard uncertainty u'_i is then calculated by dividing U'_i by a factor k, where $k = 2$ for contributions with a normal probability distribution and where $k = \sqrt{3}$ for contributions with a rectangular probability distribution.

$$u'_i = \frac{U'_i}{k} \quad (2.33)$$

The relative measurement uncertainty of the discharge coefficient u'_C for $0.2 \leq \beta \leq 0.6$ and $D < 71.12\ mm$ is calculated according to Eq. (2.34) [10]. Here the uncertainty of discharge coefficient U'_C is assumed to have a normal distribution.

$$u'_C = \frac{U'_C}{2} = \frac{1}{2}\left(0.5\% + 0.9 \cdot (0.75 - \beta)\left(2.8 - \frac{D}{25.4}\right)\right)\% \quad (2.34)$$

In the case of the experimental trials at RWTH-IOB, with the diameters and ratio given in Table 5, the relative measurement uncertainty u'_C is 0.7186%.

The relative uncertainty of the expansion number u'_ε can be described using equation (2.35) where Δp is the differential pressure at the orifice plate, p is the absolute pressure in the pipe and κ is the isentropic exponent. This uncertainty is not constant and must be calculated for data point.

$$u'_\varepsilon = \frac{U'_\varepsilon}{2} = \frac{1}{2}\left(3.5 \cdot \frac{\Delta p}{\kappa\, p}\right)\% \qquad (2.35)$$

The relative uncertainties of the pipe and throat dimensions u'_D and u'_d are determined from the uncertainty of the equipment used to measure the dimensions and the permissible variation defined in the respective ISO standard. Here the uncertainty of the pipe is assumed to be $U'_D = 0.25\%$ and of the orifice plates diameters $U'_d = 0.05\%$ Assuming a rectangular distribution of the variation of D and d, the relative uncertainties can be calculated in Eq. (2.36) and (2.37).

$$u'_D = \frac{U'_D}{\sqrt{3}} = \frac{0.25}{\sqrt{3}}\% = 0.1443\% \qquad (2.36)$$

$$u'_d = \frac{U'_d}{\sqrt{3}} = \frac{0.05}{\sqrt{3}}\% = 0.0289\% \qquad (2.37)$$

The relative extended uncertainty of the differential pressure $U'_{\Delta p}$ can be taken from the data sheet of the differential pressure sensor. Here, the relative uncertainty is 0.33% from the measured value [25]. By assuming a coverage factor of k = 2, the relative uncertainty $u'_{\Delta p}$ is 0.165%.

The relative uncertainty of the density of the gas is a function of uncertainties of the static pressure p_1, the temperature T and the gas compressibility Z according to Eq. (2.38). The uncertainties of the molar mass and the gas constant can be neglected. The uncertainties are assumed to have normal distributions.

The measurement uncertainty of the static pressure U'_{p1} is defined in the data sheet of the pressure sensor as 1% [43].[20; 43][20; 43][19; 42][18; 41][18; 40][18; 39][18; 38][18; 37][18; 36][18; 37][18; 37][18; 36]

For type N thermocouples (class 1), the tolerance is given in EN 60584-1 [10] with the greater value of ± 1.5 °C and 0. 004 · |T|. Considering a mean temperature of 20.50 °C in the pipe during the experimental tests, the absolute error of the thermocouple is assumed to be 1.5 °C and the relative error 7.32 %.

The relative uncertainty of the density is therefore:

$$u'_\rho = \frac{U'_\rho}{2} = \frac{1}{2}\left(\sqrt{{U'_{p1}}^2 + {U'_T}^2 + {U'_Z}^2}\right) = \frac{1}{2}\left(\sqrt{(0.1\%)^2 + (7.32\%)^2 + (0.1\%)^2}\right) = 3.69\% \qquad (2.38)$$

Due to the multiplicative relationship between the density and the mass flow in Eq.(2.1), the relative measurement uncertainty of the volume flow can be calculated according to (2.24).

$$u'_{qv} = \sqrt{{u'_{qm}}^2 + {u'_\rho}^2} \qquad (2.39)$$

Finally, the relative expanded uncertainty of the volume flow U'_{qv} is calculated with Eq. (2.40), with a confidence level of 95% and assuming a normal distribution:

$$U'_{qv} = 2 \cdot u'_{qv} \qquad (2.40)$$

An overview of the relative standard and expanded uncertainties of the different parameters is given in Table 11.

Table 11: Overview of the uncertainties of the volume flow calculation at the orifice plate

Parameter		Relative expanded uncertainty U'	Probability distribution -	Coverage factor k	Relative standard uncertainty $u' = U'/k$	Eq. -
Discharge Coefficient C	u'_C	1.44%	Normal	2.00	0.7186%	(2.34)
Expansibility ε	u'_ε	Variable	Normal	2.00	Variable	(2.35)
Differential pressure Δp	$u'_{\Delta p}$	0.33%	Normal	2.00	0.1650%	-
Orifice bore diameter d	u'_d	0.05%	Rectangular	1.73	0.0289%	(2.37)
Orifice inlet diameter D	u'_D	0.25%	Rectangular	1.73	0.1443%	(2.36)
Mass densityρ	u'_ρ	7.39%	Normal	2.00	3.6931%	(2.38)
Mass flow q_m	u'_{qm}	Variable	Normal	2.00	Variable	(2.32)
Volume flow q_v	u'_{qv}	Variable	Normal	2.00	Variable	(2.39)

3.4. Results and discussion

3.4.1. Impact on flow measurement

The impact of impurities on the measured flow from the Mass Flow Meter (MFM), Area Flow Meter (AFM), and Orifice Plate at three power outputs (16 kW, 20 kW, and 24 kW) is shown in Figure 12. The data is shown in relation to the density ratio of the hydrogen mixture with impurities to that of pure hydrogen. The corresponding mixtures are taken after Table 9. In addition, the set points and their corresponding uncertainties, which correspond to the volume flow of pure hydrogen set with MFC 7 in each baseline case, are also plotted. The set points for 16 kW, 20 kW and 24 kW are 5.339 m³/h, 6.674 m³/h and 8.009 m³/h respectively. The calculated measurement uncertainty of the MFM, AFM and Orifice Plate, as presented in section 3.3, are represented for each data point through error bars.

The results indicate that all three devices demonstrate good accuracy under the baseline case condition, when pure hydrogen is measured ($\rho_{Mixture}/\rho_{H_2} = 1$) . Among them, the AFM exhibits the largest deviation with volume flows up to 4.5% lower than the set point. All measurement from the MFM, AFM and orifice plate align with the set points when taking the respective measurement uncertainty into account. The deviation of the MFM remains below 1.2% while the orifice plate shows deviation of less than 2.7% for all power outputs.

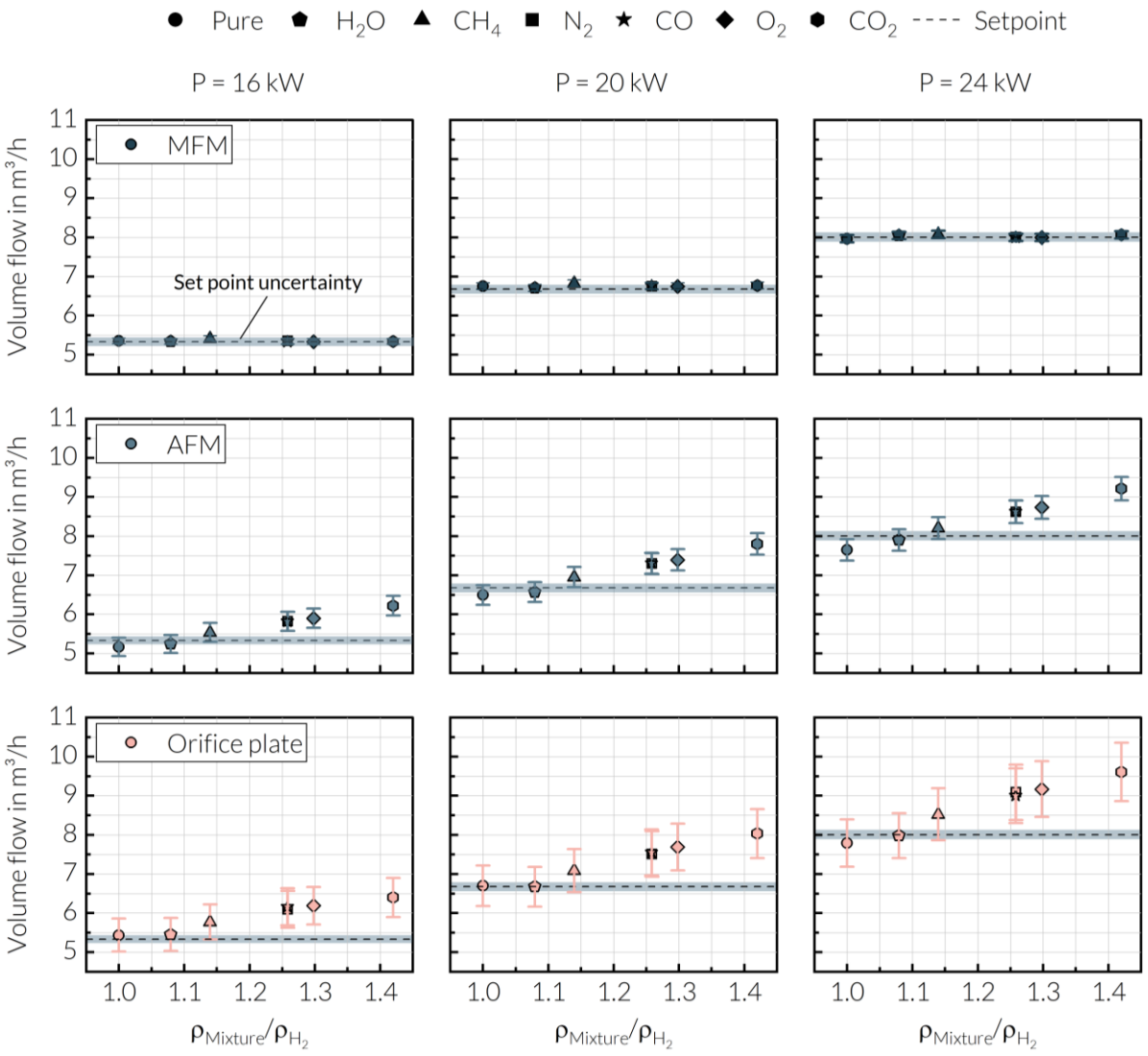

Figure 12: Volume flow measurements from the Mass Flow Meter (MFM), Area Flow Meter (AFM), and Orifice Plate, along with set points at 16 kW, 20 kW, and 24 kW power outputs in relation to the density ratio of hydrogen mixtures with impurities to pure hydrogen.

Overall the results with impurities show that the MFM achieves the highest accuracy, regardless of the impurity present in the hydrogen mixture. When considering measurement uncertainty, all data points from the MFM align with the set points.

In contrast, the AFM and orifice plate show increasing inaccuracies as the density ratio rises. Impurities with ratios $\rho_{Mixture}/\rho_{H_2}$ below 1.15, such as CH_4 and H_2O have a low impact, with measurements for both devices aligning with the set points within their measurement uncertainties. It is worth noting, that the low impact of H_2O can partially be due to its low concentration (only 1 vol% compared to 2 vol% for other impurities) in the hydrogen mixture. For mixtures with higher density ratios, such as N_2, ($\rho_{Mixture}/\rho_{H_2} = 1.258$) CO ($\rho_{Mixture}/\rho_{H_2} = 1.258$), O_2 ($\rho_{Mixture}/\rho_{H_2} = 1.297$) and CO_2 ($\rho_{Mixture}/\rho_{H_2} = 1.417$), the inaccuracies are significantly higher. The AFM consistently shows smaller deviations from the set points than the orifice plate. For hydrogen mixtures with CO_2, the data points from the orifice plate deviate by approximately 20% compared to 16% for the AFM, across all three power outputs. For impurities with comparable density ratios such as N_2 and CO, similar results are observed. For both impurities, the deviation from the AFM is approximately 9% and between 12% and 15% for the orifice plate, across all three power outputs.

To illustrate the relationship between density ratio and device inaccuracy, Figure 11 presents the deviation from the set point in percent for all three measurement devices across the different power outputs.

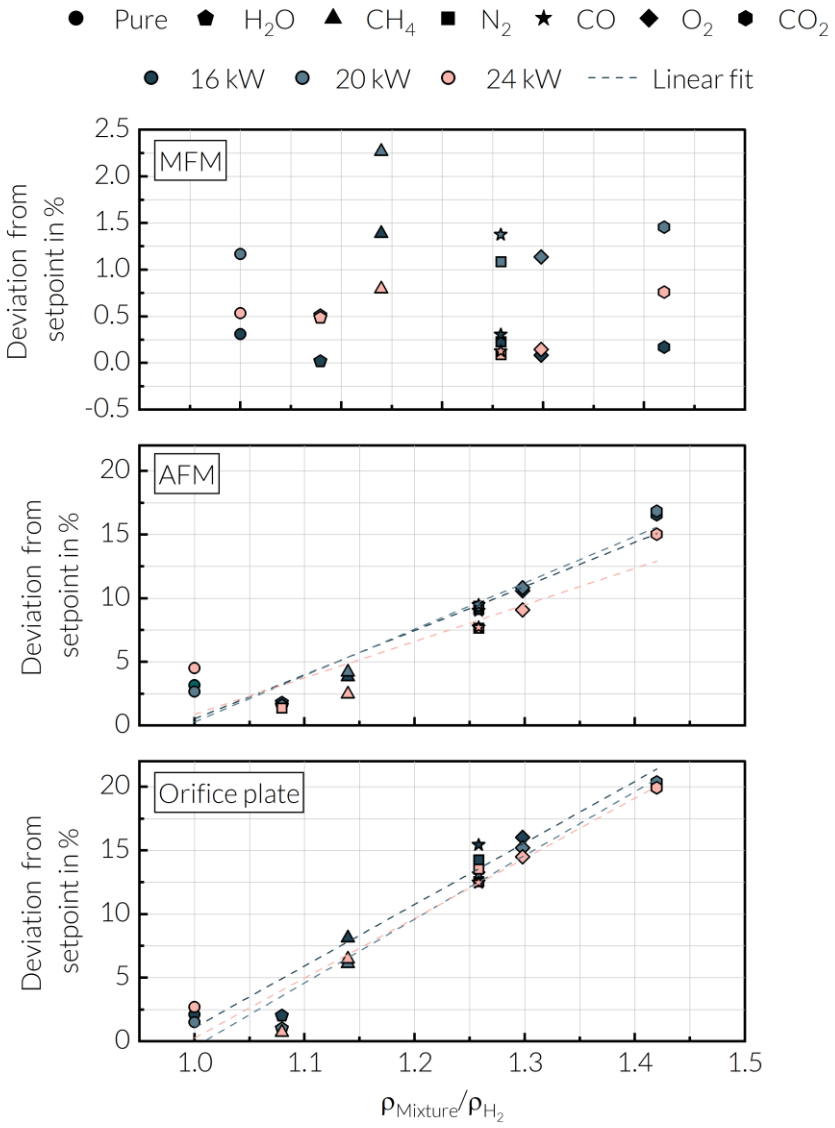

Figure 13: Deviation from the set point for the MFM, AFM and Orifice Plate at three power outputs (16 kW, 20 kW and 24 kW) in relation to the density ratio of hydrogen mixtures with impurities to pure hydrogen.

The deviation of the MFM for all data points is below 2.3%. CH_4 as an impurity leads to the highest deviation from the set point with deviations between 0.8% and 2.3%. For all other impurities, the deviation stays below 1%. For most data points, the deviation falls within the measurement uncertainties of the MFM and MFC 7 and no clear correlation between deviation and density ratio is observed. The expended measurement uncertainties of the MFM are around 1.36%, 1.24% and 1.18% for power outputs of 16, 20 and 24 kW, respectively. Additionally, the measurement uncertainty of the MFCs, which adjust the hydrogen and impurity flow have a relative uncertainty of 1.93%, 1.70% and 1.55% for 16, 20 and 24 kW, respectively.

For both the AFM and the orifice plate, a linear relationship between the density ratio and the deviation can be identified. Linear fits of the data points are presented in the corresponding diagrams for each power output. An exception to the linear trend is observed with H_2O as an impurity. However, as previously mentioned, the concentration of H_2O is only 1%, making it challenging to draw direct comparisons with the other impurities. Furthermore, the condensation of water within the pipe following humidification, as well as the presence of water droplets, cannot be excluded, contributing to the uncertainty of the data. In addition, the gradient of deviation appears lower at the orifice plate for higher volume flows.

The measurement and calculation principle of both the AFM and the orifice plate rely strongly on the density of the fluid (cf. Eqs. (2.1) and (2.9)), making these methods particularly sensitive to changes in the density of the gas mixture. As presented in Table 4, the density of the gas mixture increases between 13.9% and 41.7%, significantly affecting the measured flow rates at the orifice plate and AFM.

In contrast, the measurement principle of the MFM depends not on fluid density but on the specific heat capacity of the fluid c_p (cf. Eq. (2.11)). As discussed in section 1.3, the change in volumetric heat capacity of hydrogen with impurities is minimal, with the largest increase being 0.72% for CH_4. This correlation can also be seen in the results of the MFM, where the highest deviation is achieved for CH_4 as an impurity. Overall, the presence of impurities in hydrogen has a negligible impact on the thermal anemometry method and corresponding flow measurements.

To minimize the inaccuracy of the orifice plate for hydrogen mixtures containing impurities, one approach would be to measure the gas mixture's density within the pipe and adjust the calculated flow. This adjustment involves incorporating the changes in density (cf. Eq. (2.1)) and dynamic viscosity (cf. Eq. (2.3)) into the flow calculation. The adjustment of the dynamic viscosity would however require exact knowledge of the gas composition. Alternatively, for both the AFM and the orifice plate, inaccuracies can be reduced by applying a correction factor—a linear function dependent on the density of the impure hydrogen mixture. Considering the relationship between the volume flow q_v and the fluid density ρ_{fl} in Eq. (2.1) for the orifice plate and Eq. (2.9) for the AFM, the correction factor K_ρ can be approximated for both devices as defined in Eq. (2.41). The calculation of correction factors for AFMs can also be found in the informational materials provided by several AFM suppliers [22].

$$K_\rho = \frac{1}{\frac{\rho_{Mixture}}{\rho_{H_2}}} \cdot \sqrt{\frac{\rho_{Mixture}}{\rho_{H_2}}} = \sqrt{\frac{\rho_{H_2}}{\rho_{Mixture}}} \qquad (2.41)$$

where

ρ_{H_2} density of hydrogen used for calibration

$\rho_{Mixture}$ density of the hydrogen mixture with impurities

The adjusted volume flow is then:

$$q_{v,corr} = q_v \cdot K_\rho \qquad (2.42)$$

This method provides an approximation of the hydrogen flow. Additionally, it requires additional information about the density of the fluid, which necessitates installing a supplementary measurement system in the pipeline. Coriolis Mass Flowmeter or Ultra Sonic Flowmeter, as presented in section 4, offer good options for density measurements in the pipeline.

To demonstrate the effect of the correction factor, Figure 14 presents the corrected flow rates of the AFM and orifice plate for a power output of 20 kW. As for Figure 12, the measurement uncertainties of the devices are represented by error bars. The application of the respective correction factor to each data point significantly reduces deviations from both the setpoint and the baseline case ($\rho_{Mixture}/\rho_{H_2} = 1.0$), which was not adjusted. For all impurities except H_2O, the deviation from the baseline case ranges between 0% and 0.9% for the AFM and between 0% and 1.0% for the orifice plate. For the H_2O impurity case, the deviation is slightly higher, reaching 2.6% for the AFM and 4.1% for the orifice plate. When considering the measurement uncertainty, all adjusted flow rates align closely with the set point from MFC 7.

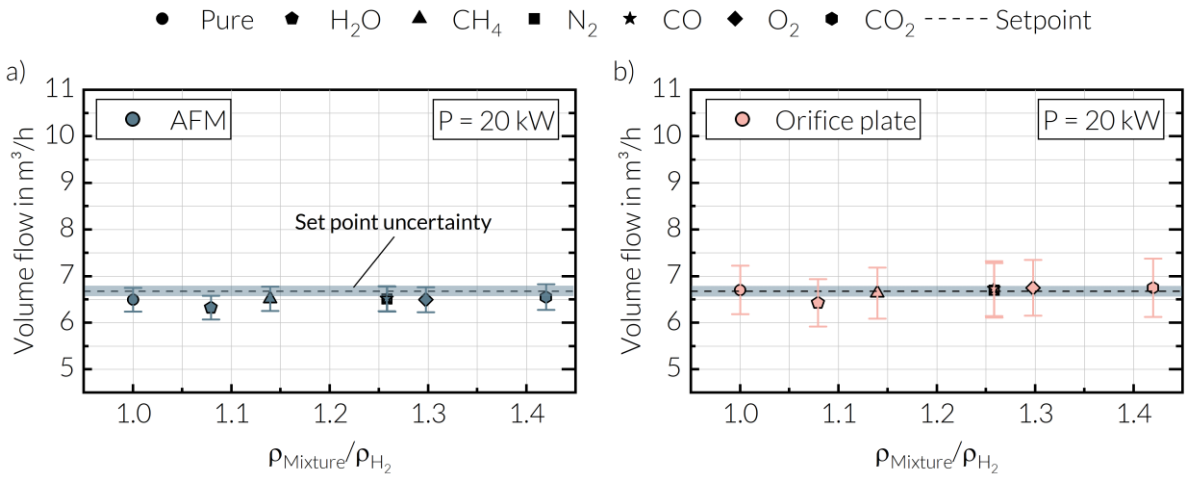

Figure 14: Adjusted volume flows for a) the AFM and b) the orifice plate of hydrogen mixtures with impurities for a power output of 20 kW in relation to the density ratio of hydrogen mixtures with impurities to pure hydrogen.

3.4.2. Impact on off-gas composition

The impact of impurities on the oxygen content in the dry off-gas is illustrated in Figure 15. In the baseline scenario, where pure hydrogen is combusted, the oxygen content in the dry off-gas was set to 3 vol% for all three power outputs. This corresponds to air flow rates of 15.1 m³/h for 16 kW, 18.38 m³/h for 20 kW and 21.65 m³/h for 24 kW power outputs. The combustion air flow was then kept constant for subsequent trials involving impurities.

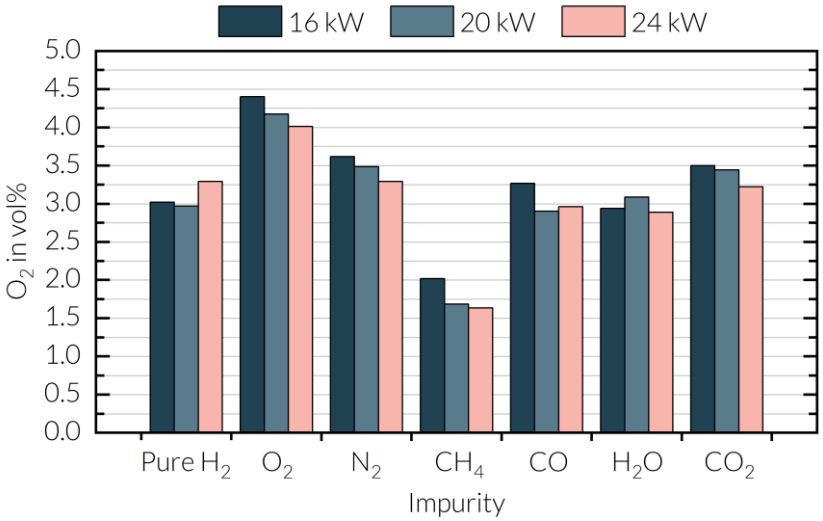

Figure 15: O_2 content in the dry off-gas for the combustion of pure hydrogen and hydrogen mixtures with 2 vol% impurities for a constant combustion air volume across the power output and at $T_{Furnace}$ = 950 °C.

Similar trends can be observed in the diagram across the different power outputs. For non-combustible impurities such as N_2, and CO_2, the oxygen content also increases, reaching values between 3.22 vol% and

3.56 vol%. This is due to the reduction in hydrogen content by 2 vol% in the mixture, requiring less oxygen for combustion. As expected, when O_2 is added as an impurity, the oxygen content in the off-gas increases above 4 vol%. This increase occurs because the mixture contains 2 vol% less hydrogen, leading to the same consequence as for non-combustible impurities and oxygen is directly introduced in the mixture, leading to a higher oxygen excess. When CO is introduced as an impurity, the change in oxygen content is negligible, as pure hydrogen and hydrogen/CO mixtures have the same minimum air requirements. In contrast, when CH_4 is added as an impurity, the oxygen content in the off-gas decreases to 1.7–2.0 vol%. This is because CH_4 is combustible and its mixture with hydrogen has a 6% higher minimum air requirement than pure hydrogen, resulting in greater oxygen consumption during combustion.

The change in oxygen content and air ratio is illustrated in Figure 16, showing their correlation with the ratio of the minimum air requirement for hydrogen mixtures with impurities to that of pure hydrogen, for a constant power output of 20 kW.

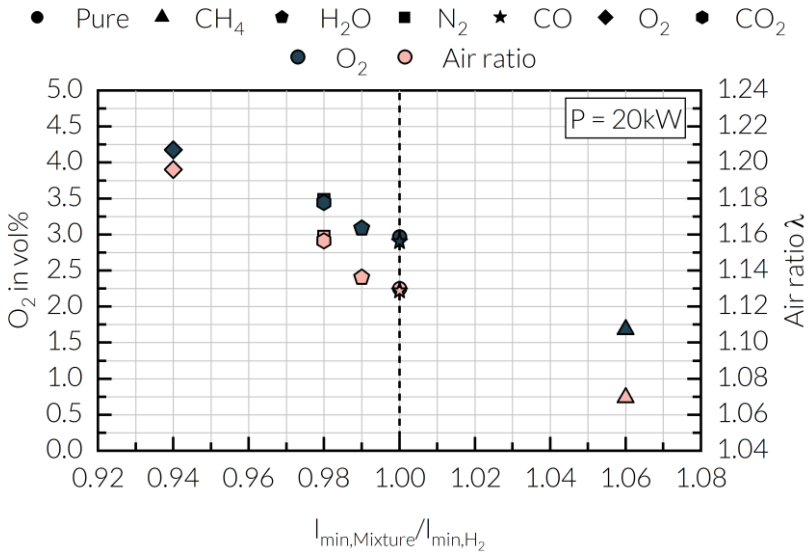

Figure 16: Change in O_2 content in the dry off-gas and air ratio for the combustion of pure hydrogen in relation with the ratio of minimum air requirement of the mixture to that of hydrogen for a power output of 20 kW.

The air ratio λ is calculated from the oxygen content in the off-gas according to Eq. (2.43) [36]:

$$\lambda = 1 + \frac{y_{o_2,dry}}{0.21 - y_{o_2,dry}} \cdot \frac{v_{A,min,tr}}{l_{min}} \qquad (2.43)$$

where

$y_{o_2,dry}$ Oxygen content in the dry off-gas (measured)

$v_{A,min,tr}$ Min. dry off-gas volume of the gas mixture

l_{min} Min. air requirement of the gas mixture

For pure hydrogen, the measured O_2 content in dry off-gas is 2.97 vol%, and the corresponding air ratio is 1.13. When impurities are introduced, a linear correlation between the minimum air requirement ratio and the oxygen content can be observed. As previously mentioned, impurities that reduce the minimum air requirement ratio below 1 — such as H_2O ($l_{min,Mixture}/l_{min,H_2} = 0.99$), N_2 ($l_{min,Mixture}/l_{min,H_2} = 0.98$), CO_2 ($l_{min,Mixture}/l_{min,H_2} = 0.98$), and O_2 ($l_{min,Mixture}/l_{min,H_2} = 0.94$) — result in a higher oxygen content in the off-gas: 3.09 vol%, 3.49 vol%, 3.44 vol%, and 4.17 vol%, respectively. Similar trends are observed for the air ratio and a linear correlation between air ratio and minimum air requirement ratio can also be observed. For these impurities, the air ratio λ increases to 1.136, 1.159, 1.157, and 1.196 for H_2O, N_2, CO_2, and O_2, respectively. When methane is added ($l_{min,Mixture}/l_{min,H_2} = 1.060$), the oxygen content decreases to

1.69 vol%, and the air ratio drops to 1.070. Therefore, oxygen and methane impurities have the most significant impact on oxygen content in the dry off-gas.

In addition to the investigation of the impact of impurity admixtures on the oxygen content, their effects on CO, CO_2, and H_2O in the dry off-gas were also analysed. Figure 17 shows the CO content in the dry off-gas for the three power output levels. Overall, the CO concentration is very low, remaining below 0.02 vol% for all cases. Since the resolution of the analyser is 0.01%, the results should be interpreted cautiously due to the relatively high measurement error.

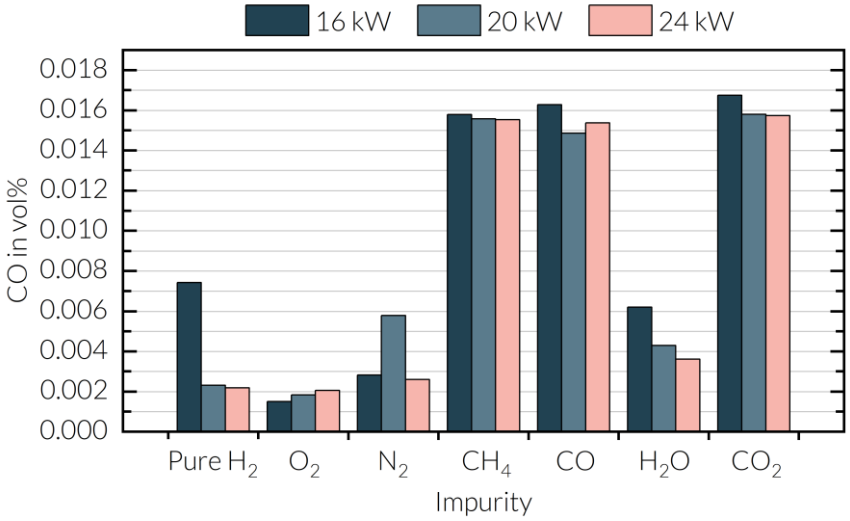

Figure 17: CO content in the dry off-gas for the combustion of pure hydrogen and hydrogen mixtures with 2 vol% impurities for a constant combustion air volume across the power output and at $T_{Furnace}$ = 950 °C.

For the combustion of pure hydrogen, the CO content in the dry off-gas is below 0.008 vol%. Overall, all measured data points are below 0.02 vol%. The accuracy of the analyser however is 0.05 vol%, suggesting limitations in the accuracy of the measured data. When burning pure hydrogen, no CO should be present in the off-gas. Since the furnace is initially heated with natural gas, residual CO and CO_2 may remain in the analyser and furnace chamber even after switching to hydrogen combustion. The presence of unburned CO is however questionable.

Introducing impurities containing carbon — such as CH_4, CO, and CO_2 — causes a slight increase, with CO concentrations rising to approximately 0.015 vol% across all three species and power outputs. The influence of H_2O on CO content is more challenging to evaluate; while an increase of up to 0.006 vol% can be observed, this value falls within the analyser's accuracy limit. Moreover, it is unclear why the addition of CO_2 as an impurity would lead to a higher CO concentration. One possible explanation for this phenomenon is the shift of the Boudouard equilibrium (Eq. (2.45)) at high temperatures. At a furnace temperature of 950 °C, the equilibrium favours the reverse reaction of CO_2 to CO.

$$C + CO_2 \leftrightarrow 2\,CO \qquad (2.44)$$

Figure 18 shows the CO_2 content in the dry off-gas for the three power output levels. For the baseline case, when pure hydrogen is combusted, the CO_2 content is below 0.4 vol% for a power of 16 kW and below 0.21 vol% for 20 kW and 24 kW. As for CO, it is questionable why CO_2 is present during the combustion of pure hydrogen. Overall similar results as for CO can be observed for CO_2.

Carbon free impurities such as O_2 and H_2O lead to no change in CO_2 emissions, while impurities containing carbon such as CH_4, CO and CO_2 lead to an increase in CO_2 in the off-gas up to values between 0.8 vol% and 0.98 vol%. Theoretical calculations of the dry off-gas composition for an air ratio of λ = 1.13 indicate CO_2 content of 0.92%, 0.9% and 0.9% for CH_4, CO and CO_2 respectively. The measured values align closely with these calculations, confirming the measurement accuracy.

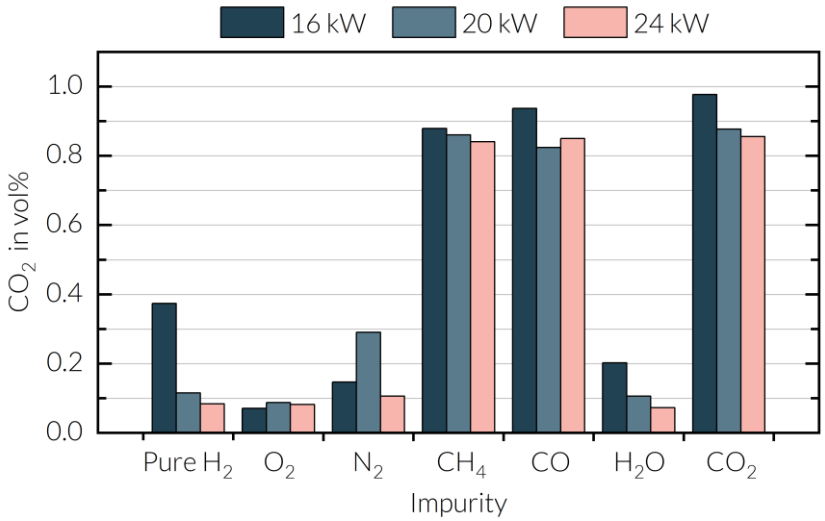

Figure 18: CO_2 content in the dry off-gas for the combustion of pure hydrogen and hydrogen mixtures with 2 vol% impurities for a constant combustion air volume across the power output and at $T_{Furnace}$ = 950 °C.

Figure 19 shows the impact of impurities on the H_2O content in the off-gas compared to pure hydrogen combustion. Across all data points, the H_2O content ranges between 27.2 vol% and 30.3 vol%. Notably, the H_2O content in the off-gas increases with increasing power output, although this observation is questionable as the power output should theoretically have no influence on the off-gas composition.

Across all impurity cases, the average increase in water content is about 1.7% between 16 kW and 20 kW and about 4.2% between 16 kW and 24 kW. Theoretical calculation for pure hydrogen combustion at an air ratio of λ = 1.13 indicate a water content of about 31.3 vol%. However, the measured values are lower by about 11%, 8% and 7% for power outputs of 16 kW, 20 kW and 24 kW respectively. This indicates that water may have condensed in the extraction pipe during the measurement, making the results unreliable.

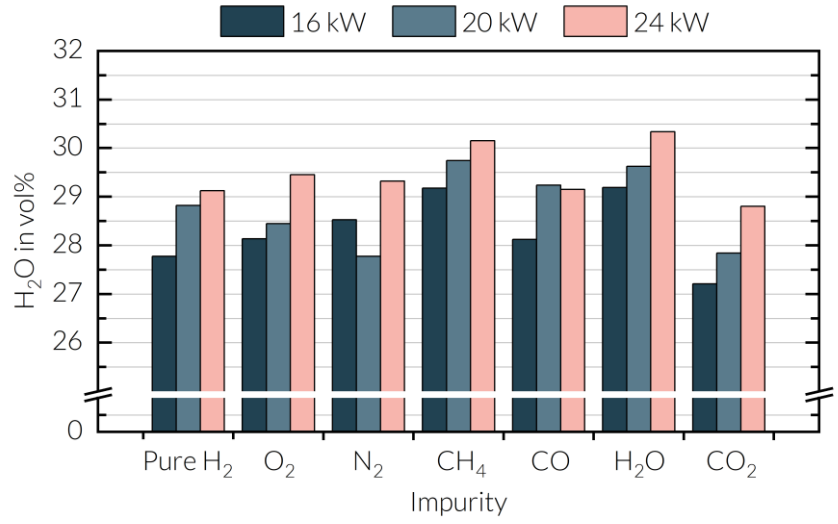

Figure 19: H_2O content in the dry off-gas for the combustion of pure hydrogen and hydrogen mixtures with 2 vol% impurities for a constant combustion air volume across the power output and at $T_{Furnace}$ = 950 °C.

Theoretical calculations show that the impurities N_2, O_2 and CO_2 reduce the H_2O content by 2.31% compared to the baseline condition. For N_2 and O_2 show, the measured values show no consistent trend: in some cases, the H_2O content increases, while in others it decreases, with variation ranging from -3.6% to

+2.7%. On the contrary, CO_2 as an impurity consistently decreases the H_2O content with reductions of up to -2.0 % for 16 kW, -3.4% for 20 kW and -1.1vol% for 24 kW compared to pure hydrogen combustion.

When H_2O itself is added as an impurity, the water content in the off-gas increases by up to 5.1% at 16 kW, 2.8% at 20 kW and 4.2% at 24kW. However, theoretical calculations of moist off-gas composition suggest that adding H_2O as an impurity should have almost no effect on the water content in the off-gas. Finally, while the addition of CO as an impurity is expected to reduce the water content by 2%, the measured values show a slight increase ranging from 0.1% to 1.4%, compared to the baseline condition. Overall, the observed changes in off-gas water content deviate from theoretical calculations, except in the case of CO_2 as an impurity, which aligns with the expected changes.

3.4.3. Impact on pollutant emissions

The effect of impurities on pollutant emissions such as nitrogen oxides (NO_x) are shown in Figure 20, with measurements reported in $mg/m^3_{Offgas,\ dry}$. Overall, the data indicate that NO_x emissions decrease as the burner's power output increases. One reason for this behaviour could be that the nominal power of the burner is 50 kW. However, in this study, the burner's power output was limited to a range of 16 to 24 kW. Operating the burner below its nominal power can result in reduced flow velocities at the burner outlet, potentially affecting its optimal adjustment for minimizing NO_x emissions. Despite these variations in power output, the trends in NO_x emissions were consistent across different impurities, indicating that the observed behaviour is independent of the specific power output within the studied range.

In the baseline case, when pure hydrogen is combusted, NO_x emissions are approximately 305 $mg/m^3_{Offgas,\ dry}$ at a power output of 16 kW, 266 $mg/m^3_{Offgas,\ dry}$ at 20 kW and 216 $mg/m^3_{Offgas,\ dry}$ at 24 kW. Adding O_2 as an impurity, leads to an increase in NO_x emissions by 32-37% across the different power outputs. This increase is attributed to the strong influence of oxygen on thermal NO formation, as a higher oxygen content in the gas-air mixture increases the adiabatic flame temperature up to 2098 °C (cf. Table 4), thereby promoting NO formation. In contrast, the addition of impurities such as N_2, CO, and CO_2 results in a minimal decrease in NO_x emissions, typically by 1–2%. This behaviour can be explained by the inert behaviour of N_2 and CO_2, which do not significantly react with the gas-air mixture and thus have little impact on the combustion process. Similarly, CO is oxidized to CO_2 during combustion without directly influencing the NO formation mechanism. In addition, the impurities lead to a slight decrease in adiabatic flame temperature of the mixture. The addition of CH_4 as an impurity reduces NO_x emissions by 13–15% across the different power outputs. This reduction is due to the lower reactivity, adiabatic flame temperature, and laminar flame velocity of CH_4 compared to hydrogen. These properties could result in a lower flame temperature, which slows down the formation of thermal NO. Finally, the addition of H_2O leas to a slight increase in NO_x emissions of about 3%, 2% and 6% for 16 kW, 20 kW and 24 kW respectively.

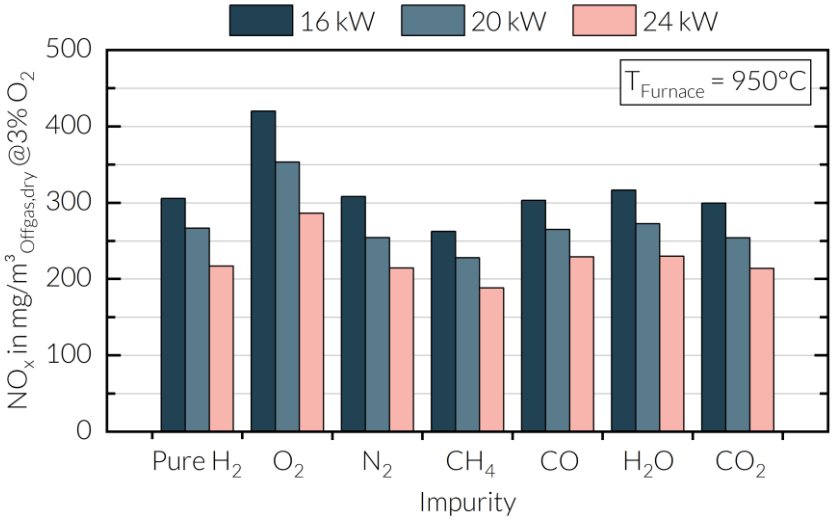

Figure 20: NO_x emissions in the dry off-gas for the combustion of pure hydrogen and hydrogen mixtures with 2 vol% impurities for a constant combustion air volume across the power output and at $T_{Furnace}$ = 950 °C.

4. H_2 quality estimation using a prototype SICK Ultra-Sonic H_2 Flow Meter

4.1. Speed-of-sound-based algorithms for H_2 quality estimation

4.1.1. Basics

Ultrasonic flow meters (USM) need to measure the speed of sound of the flowing medium with very high accuracy. Since the speed of sound (SOS) is gas dependent, it can be used for diagnostic purposes such as gas quality estimation. For example, some SICK USMs use SOS-based algorithms for estimating the quality of natural gas [39]. Similar algorithms can also be used for estimating the purity of hydrogen.

H_2 has a much higher speed of sound than all relevant gases that can appear as impurities in most applications (Table 12). Adding only small amounts of these gases to pure hydrogen leads to a significant reduction of the speed of sound of the mixture (Figure 21). It is therefore possible to detect and estimate very low quantities of impurities by using algorithms that compare the SOS measured by the USM to the expected SOS of pure hydrogen. Two such algorithms have been developed and tested by SIEN as part of work package 4, task 4.1 of the HyInHeat project. One uses easy to compute pre-trained models, which makes it suitable for devices with a focus on low power consumption and also for older devices with low computing power. The other uses a suitable equation of state (EOS) for gas mixtures, e.g. GERG-2008 [32], integrated into the device firmware. This makes the algorithm harder to compute but enables more possibilities in terms of process conditions and gas species.

Both algorithms use the SOS measured by the USM, as well as measurements of temperature and pressure of integrated sensors, and estimate the molar fractions of hydrogen and the known impurity gas. Additional properties like heating value or Wobbe index can then be calculated using established methods like ISO 6976.

Table 12: Speed of sound of H_2 and common impurity gasses

Species	H_2	CH_4	O_2	N_2	CO	CO_2
SOS [m/s] @ T= 20°C, p=1bar(a)	1305	445	326	349	349	267

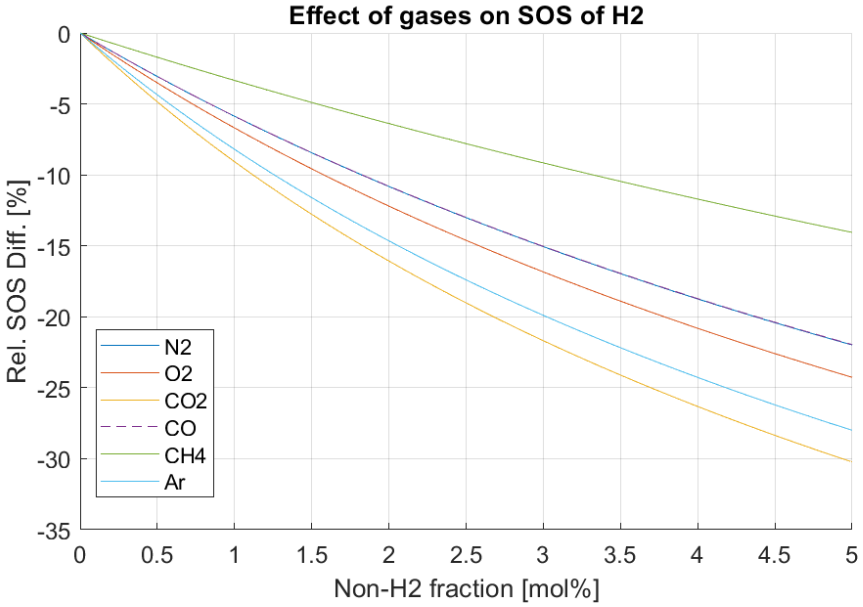

Figure 21: Effect of different impurity gases on the speed of sound of hydrogen.

4.1.2. Model-based algorithm

The first algorithm for H_2 purity estimation is illustrated in Figure 22. It uses two easy to compute pre-trained models. This makes it suitable for devices with a focus on low power consumption and also for older devices with low computing power.

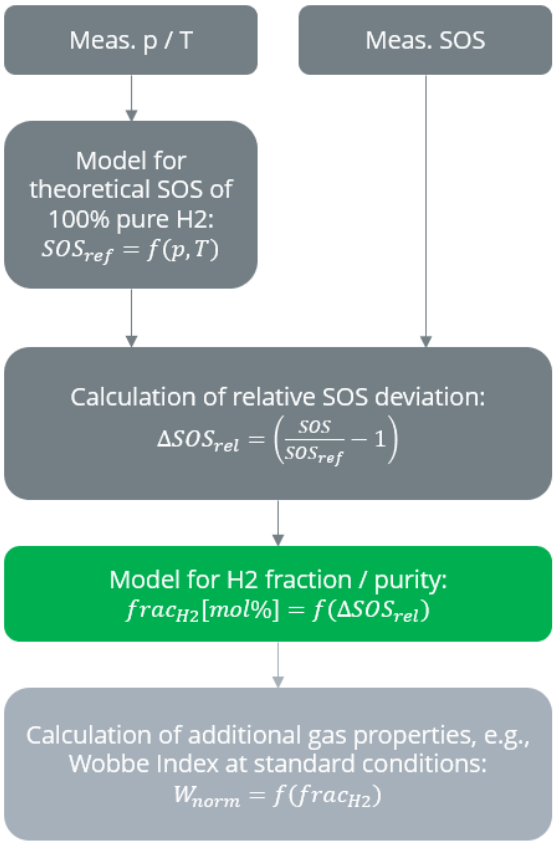

Figure 22: Model-based algorithm for H_2 purity estimation.

The first model is a 2D polynomial of second order that uses the measured values for pressure (p) and temperature (T) to continuously calculate the theoretical SOS of pure hydrogen at process conditions (SOS_{ref}):

$$SOS_{ref} = f_1(p[MPa], T[K]) \tag{2.45}$$

with

$$f_1\colon (p,T) \rightarrow CC_{00} + CC_{10} * p + CC_{01} * T + CC_{20} * p^2 + CC_{11} * p * T + CC_{02} * T^2 \tag{2.46}$$

The six model coefficients CC_{ij} were obtained by fitting data generated with the Gerg-2008 state equation on a grid covering the relevant temperature and pressure ranges of -25…85 °C and 5…100 bar(g) respectively.

The theoretical SOS of pure hydrogen calculated by model f_1 is compared to the actual SOS measured by the ultrasonic flow meter. The relative deviation of these two values

$$\Delta SOS_{rel}[\%] = 100 \cdot \left(\frac{SOS}{SOS_{ref}} - 1\right) \tag{2.47}$$

is calculated and used as the input for a second pretrained model f_2, which estimates the fraction / purity of hydrogen in the gas mixture:

$$frac_{H2}[mol\%] = f_2(\Delta SOS_{rel}) \tag{2.48}$$

with

$$f_2\colon x \to 100 * (CC_0 + CC_1 * x + CC_2 * x^2 + CC_3 * x^3 + CC_4 * x^4 + CC_5 * x^5) \tag{2.49}$$

To achieve sufficient accuracy, this model must be trained for the specific impurity relevant for the application. For example, one would need to use a different set of coefficients CC_i for nitrogen than for methane.

4.1.3. Optimization algorithm

The second algorithm (illustrated in Figure 23) uses a suitable equation of state (EOS) for gas mixtures, e.g., GERG-2008, integrated into the device firmware. The measured values by the USM are again SOS, p, and T. Additionally, initial guesses for the hydrogen and pollutant fractions are used as starting values for the calculation. A 50:50 guess is sufficient, but the type of pollutant gas must be accurate for the algorithm to work with low uncertainty. The SOS of the starting gas composition is calculated at the measured pressure and temperature using the EOS integrated into to device firmware and the relative deviation ΔSOS to the SOS measured by the USM is calculated. Subsequently, a simple gradient descent-based optimization is used to minimize ΔSOS by changing the hydrogen fraction. The algorithm stops when the relative difference between calculated and measured SOS is smaller than 0,1%. The algorithm typically converges after only two or three iterations. With the optimized molar fractions of hydrogen and impurity gas the output values relevant to the application can be calculated using the EOS.

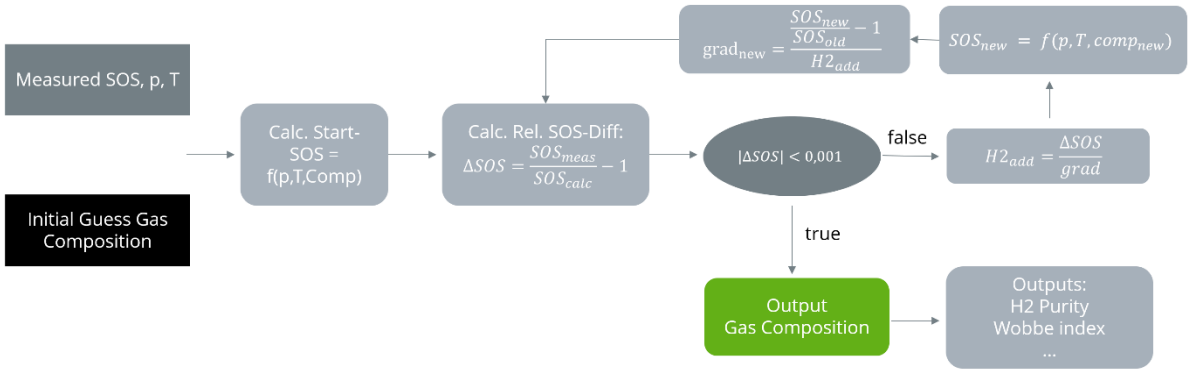

Figure 23: Optimization algorithm for H_2 purity estimation.

4.2. Numerical uncertainty simulation

4.2.1. Uncertainty contributions

Assuming that the correct gas specific model for the H_2 fraction estimation is used, the following sources of uncertainties need to be considered:

- Uncertainty of temperature measurement: $\sigma_T = \pm 0.5K$
- Uncertainty of pressure measurement: $\sigma_p = \pm 0.3\%$
- Uncertainty of speed of sound measurement: $\sigma_{SOS} = \pm 0.1\%$
- Uncertainty of H_2 SOS reference data (GERG): $3\sigma_{GERG\_SOS} < \pm 0.02\%$

The given values for the uncertainty of temperature and pressure measurement are chosen conservatively based on typical available sensors.

The assumed uncertainty of the speed of sound measurement of 0.1 % is also typical for USMs and could even be further reduced by calibrating the device with pure hydrogen. The uncertainty of the speed of sound reference data generated using the GERG-2008 state equation is estimated by a comparison against NIST data on hydrogen. It is generally much lower than the uncertainty of the measured SOS and is therefore not significant.

4.2.2. Numerical uncertainty simulation

The total uncertainty of both H_2 purity algorithms can be simulated numerically using random number generation. For a single process point defined by temperature (T_{ref}), pressure (p_{ref}) and H_2-Fraction ($frac_{H2}^{ref}$), 100 randomized sets of model inputs are drawn from a normal distribution with the appropriate standard deviation (denoted as Matlab syntax $randn$):

$$T_{meas,i} = T_{ref} + randn(\sigma_T = 0.5K) \quad (2.50)$$

$$p_{meas,i} = p_{ref} * (1 + randn(\sigma_p = 0.3\%)) \quad (2.51)$$

$$SOS_{meas,i} = SOS_{GERG}(p_{ref}, T_{ref}) * (1 + randn(\sigma_{SOS} = 0.1\%)) \quad (2.52)$$

For each set of inputs, the estimated H_2 fraction ($frac_{H2}^{Est.}$) is calculated using the algorithms described in section 4.1.

The error of the outputs can then be calculated:

$$Err_{abs}[mol\%] = frac_{H2,i}^{Est.} - frac_{H2}^{ref} \quad (2.53)$$

This is done for 100 sets of inputs for every process point on the following grid:

- $T_{ref} \in [-25°C, 85°C]$ with steps of $5\ K$
- $p_{ref} \in [5bar, 100bar]$ with steps of $5\ bar$
- $frac_{H2}^{ref} \in [95mol\%, 100mol\%]$ with steps of $0.1mol\%$

The result is a distribution of the model error consisting of 1 380 000 data points and fully covering the relevant range of process conditions.

Figure 24 contains an example error distribution for the estimated H_2 fraction with nitrogen as the impurity using the model-based algorithm. The resulting uncertainty assuming 95% confidence is roughly $2\sigma \approx 0.05mol\%$.

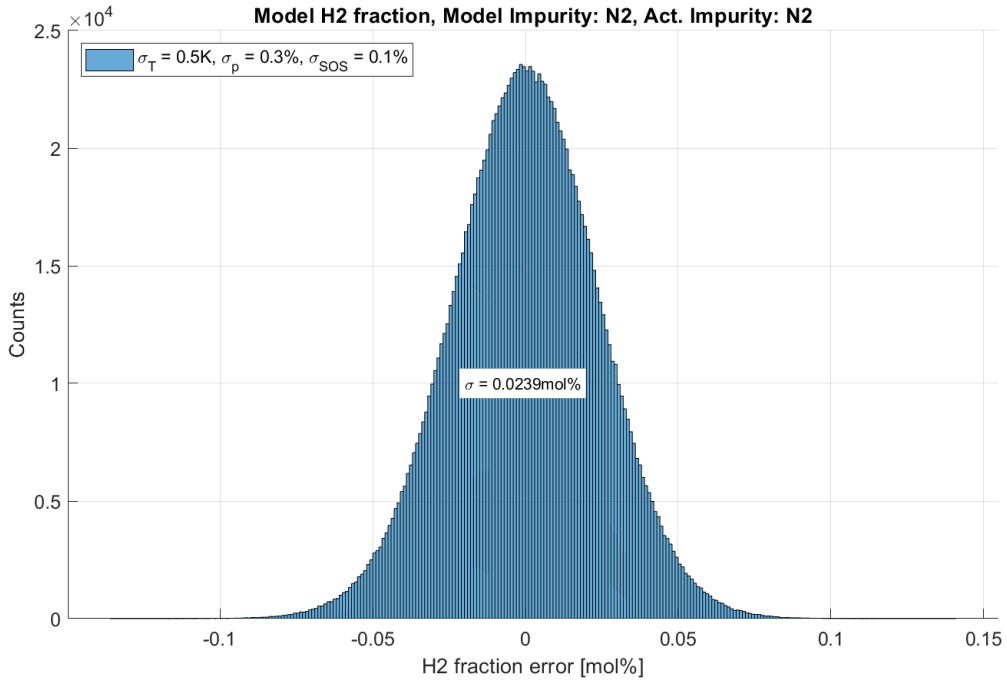

Figure 24: Simulated error distribution of the model-based algorithm with N_2 as impurity gas.

Table 13 contains the resulting uncertainties for both algorithms and different impurity gases.

Table 13: Simulated uncertainties of the algorithms for different impurity gasses.

Species	N_2	O_2	CO_2	CO	CH_4
Unc. (2σ) [mol%] Model-based Alg.	0.048	0.042	0.032	0.048	0.084
Unc. (2σ) [mol%] Optimization Alg.	0.052	0.048	0.040	0.086	0.044

4.3. Experimental Verification

Testing of the developed H_2 purity algorithms in a prototype SICK USM for H_2 applications was initially planned to be carried out at the experimental setup at RTWH-IOB. But due to the small line sizes and low flow rates it was later concluded that a prototype USM with a line size of at least 2" / DN50 is not feasible for the setup. Additionally, because of acoustic reasons a line size of at least 4" / DN100 would be preferable for testing the H_2 algorithms. It was therefore decided that the experimental testing of the algorithms would instead be done with static measurements at SIEN.

The primary goal of the measurements is to demonstrate the algorithms with real measurement data and verify the uncertainties predicted by the simulations described in section 4.2. Nitrogen and Methane were used as impurity gasses for the tests.

4.3.1. Prototype H_2 USM

A 4" / DN100 prototype USM for H_2 measurement was built for the H_2 purity measurements (Figure 25). The device uses 8 ultrasonic measurement paths featuring prototype H_2 transducers that are currently in development by SIEN. The USM has an integrated pressure and temperature sensor, as well as an additional high accuracy class A PT1000 temperature sensor to accurately measure the gas temperature near the plane of measurement of the ultrasonic paths. Before the measurements the device was zero flow calibrated using H_2 with a purity of >99.999mol%.

Figure 25: 4" SICK Prototype USM or H_2 measurements.

4.3.2. Experimental Setup

Figure 26 shows some photos of the experimental setup. The measurements took place outside due to safety reasons. A simple pipe crossing with ball valves is used to fill the meter body with either hydrogen or the impurity gas and to be able to release the pressure through an exhaust hose.

At the start of each measurement series the USM is filled with hydrogen with a purity >99.999%. This is achieved by repeatedly filling the device with hydrogen at a pressure of at least 10 bar(a) and then releasing it back to ambient pressure. After five cycles of this process, the purity within the device should match the

purity supplied by the gas bottle. Next, the piping leading to the sealed USM is flushed and then filled with the impurity gas at a slightly higher pressure than that inside the USM. The valves to the gas bottles are then closed, and the valve to the USM is opened. Due to the significantly smaller volume of the piping compared to the USM, only a minimal amount of impurity gas enters the meter body, causing a slight increase in pressure.

This slight increase in pressure caused by the added impurity gas is measured by an independent calibrated high accuracy pressure sensor (Elgas EDT 96 [12], accuracy <0.25%, repeatability <0.01%). With the pressure readings before and after adding the impurity gas the molar fractions of hydrogen and impurity can be calculated using Dalton's Law [11] as is further explained in section 4.3.3. The molar fractions calculated this way serve as independent reference values for the H_2 algorithms.

This process of adding very small amounts of impurity gas is repeated several times to cover a practically relevant range.

Figure 26: Test setup for H_2 purity measurements at SIEN.

4.3.3. H_2 / N_2 Experiment

Figure 27 shows the measured values for SOS, p and T over the course of the measurement with N_2 as impurity gas. At the start the USM was filled with ~20.7 bar(a) H_2 with a purity >99.999 mol%. Nitrogen was added in five steps, as described in section 4.3.2., each time leading to a slight increase in pressure and reduction of the speed of sound measured by the USM.

With the pressure increase Δp_i of each step the reference molar fractions of hydrogen $frac_{H2_i}^{ref}$ and nitrogen $frac_{N2_i}^{ref}$ are calculated:

$$p_i^{after} = p_i^{before} + \Delta p_i \tag{2.54}$$

$$frac_{H2_i}^{ref} = frac_{H2_{i-1}}^{ref} \cdot \frac{p_i^{before}}{p_i^{after}} \tag{2.55}$$

$$frac_{N2_i}^{ref} = 1 - frac_{H2_i}^{ref} \quad (2.56)$$

Due to fluctuations in ambient temperature during the day, the gas temperature inside the USM was also variable, as shown in Figure 27. These temperature result in pressure gradients that need to be compensated to accurately calculate the molar fractions after each step. This compensation is achieved by linear extrapolation of the pressure gradients underlying each pressure increase Δp_i as shown in Figure 28.

Table 14 contains the compensated pressure measurements and the calculated molar fractions of H_2 and N_2 for each step. The uncertainty of these values is hard to estimate accurately because of the unstable ambient conditions during the tests. However, considering the resolution and repeatability of the pressure sensor and the fact that only pressure ratios and differentials are used in the calculation, the uncertainty should be in the same order of magnitude as the SOS-based algorithms.

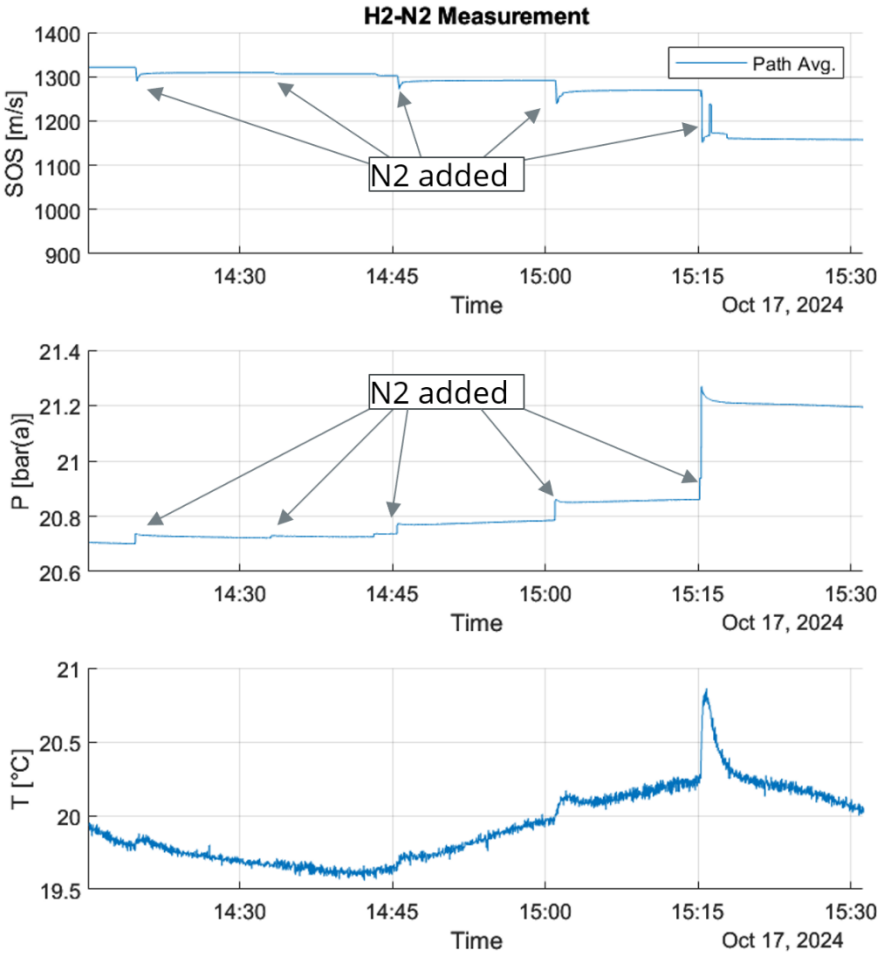

Figure 27: Measured SOS, p and T over the course of the H_2/N_2 experiment.

Table 14: Reference molar fractions calculated via pressure change (H_2/N_2).

Step	p_{before} $[bar(a)]$	Δp $[bar(a)]$	$frac_{H2}^{ref}$ $[mol\%]$	$frac_{N2}^{ref}$ $[mol\%]$
0	-	-	>99.999	<0.001
1	20.6950	0.0314	99.848	0.152
2	20.7196	0.0078	99.811	0.189
3	20.7268	0.0425	99.607	0.393
4	20.7892	0.067	99.312	0.688
5	20.8607	0.3428	97.689	2.311

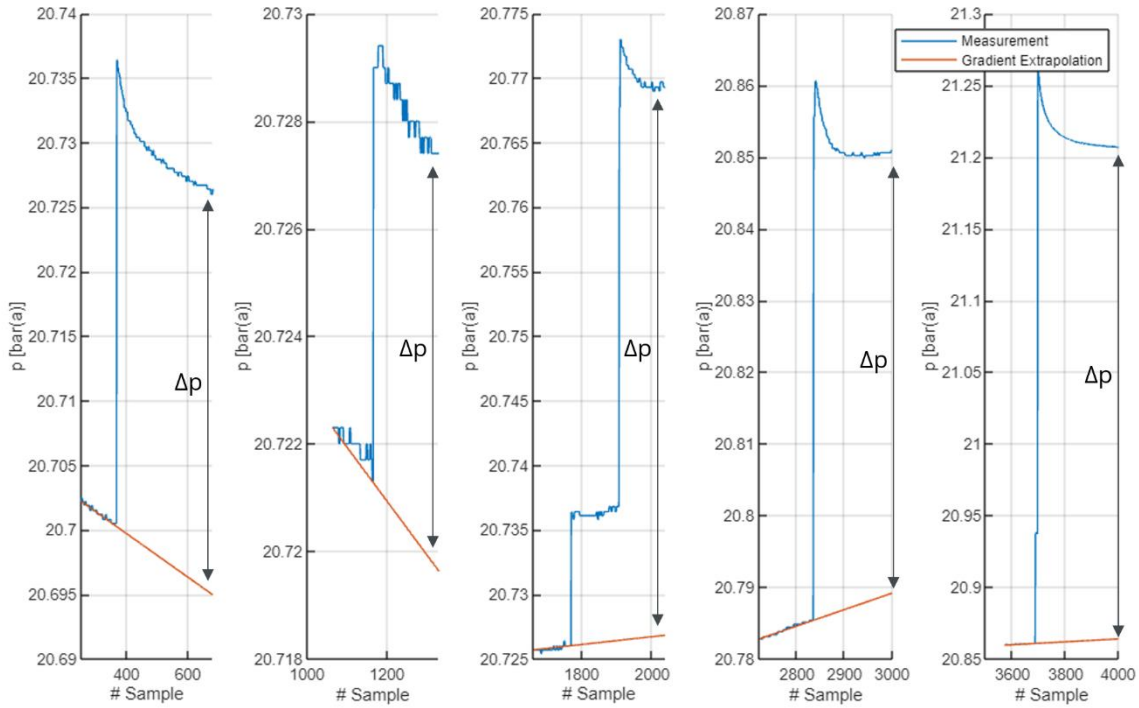

Figure 28: Pressure change correction by linear compensation of underlying pressure gradients.

The input measurements as well as the results of the two SOS-based H_2 purity algorithms are shown in Table 15. The model-based algorithm was running in the firmware of the device during the measurement whereas the optimization algorithm was evaluated after the measurements using data logs. The deviation of both algorithms to the reference molar fractions calculated via pressure change is shown in Table 16.

Both algorithms give practically identical results. The deviation to the independently calculated reference values is <±0.05mol% over the measured range of between 97.6 and 100 mol% H_2 purity. This in very good agreement with the simulations explained in section 4.2.

The second step where N_2 was added is especially interesting, because only <0.04mol% of N_2 were added to the gas mixture. As shown in Figure 29, such small and even smaller changes in H_2 purity can easily be detected by measuring the change of the SOS.

Table 15: Results of the two H_2 purity algorithms denoted by the uppercase index "Mod." for the model-based algorithm and "Opt." for the optimization algorithm (H_2/N_2).

Step	p_{USM} [$bar(a)$]	T_{USM} [$°C$]	SOS_{USM} [m/s]	$frac_{H2}^{Mod.}$ [$mol\%$]	$frac_{H2}^{Opt.}$ [$mol\%$]
0	20.701	19.80	1321.38	100.01	99.99
1	20.722	19.67	1309.26	99.87	99.86
2	20.726	19.61	1306.34	99.83	99.83
3	20.785	19.97	1291.92	99.64	99.64
4	20.860	20.23	1269.72	99.35	99.35
5	21.195	20.04	1157.92	97.64	97.64

Table 16: Deviation of the two H_2 purity algorithms to the reference molar fractions calculated via pressure change (H_2/N_2).

Step	$Deviation_{H2}^{Mod.}$ [$mol\%$]	$Deviation_{H2}^{Opt.}$ [$mol\%$]
0	<0.01	<0.01
1	0.022	0.012
2	0,019	0.019
3	0.033	0.033
4	0.038	0.038
5	-0.049	-0.049

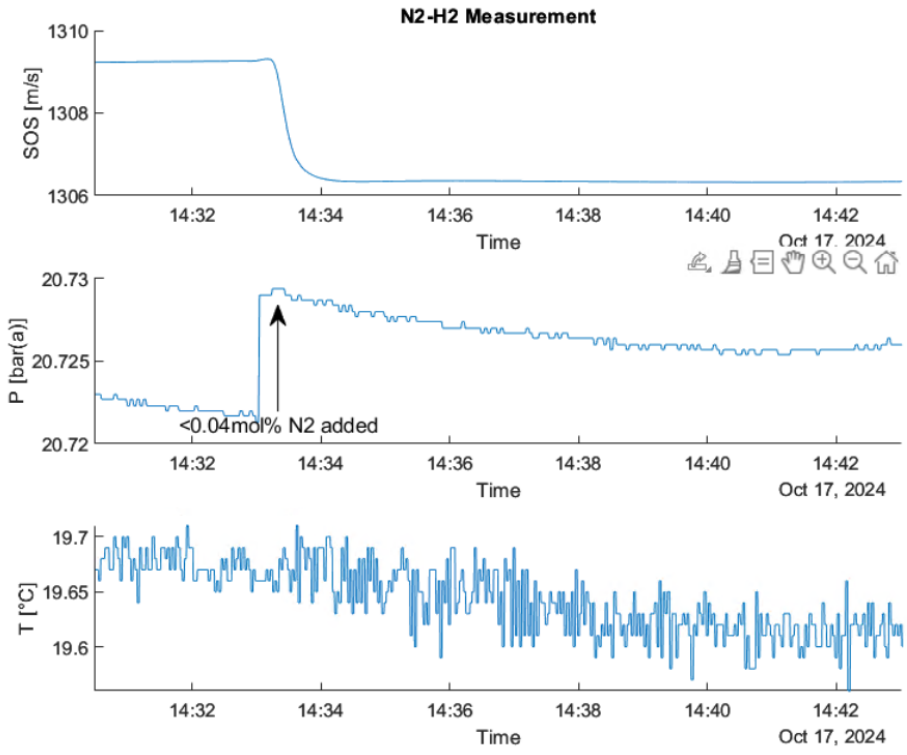

Figure 29: Detailed view of the smallest pressure change (step 2).

4.3.4. H_2 / CH_4 Experiment

The measurement with methane as impurity gas were done and evaluated in the same way as the nitrogen measurements described in section 4.3.3. At the start the USM was filled with ~10 bar(a) of hydrogen. CH_4 was added in three steps to a total amount of ~6.9 mol%. Figure 30 shows the timeline of the test. The reference molar fractions based on the pressure measurements before and after the steps are contained in *Table 17*. Table 18 shows the results of the two SOS-based H_2 purity algorithms and the deviation to the reference values.

Again, both algorithms give almost identical results and the deviation to the independent reference values is in excellent agreement with the simulations described in section 4.2.

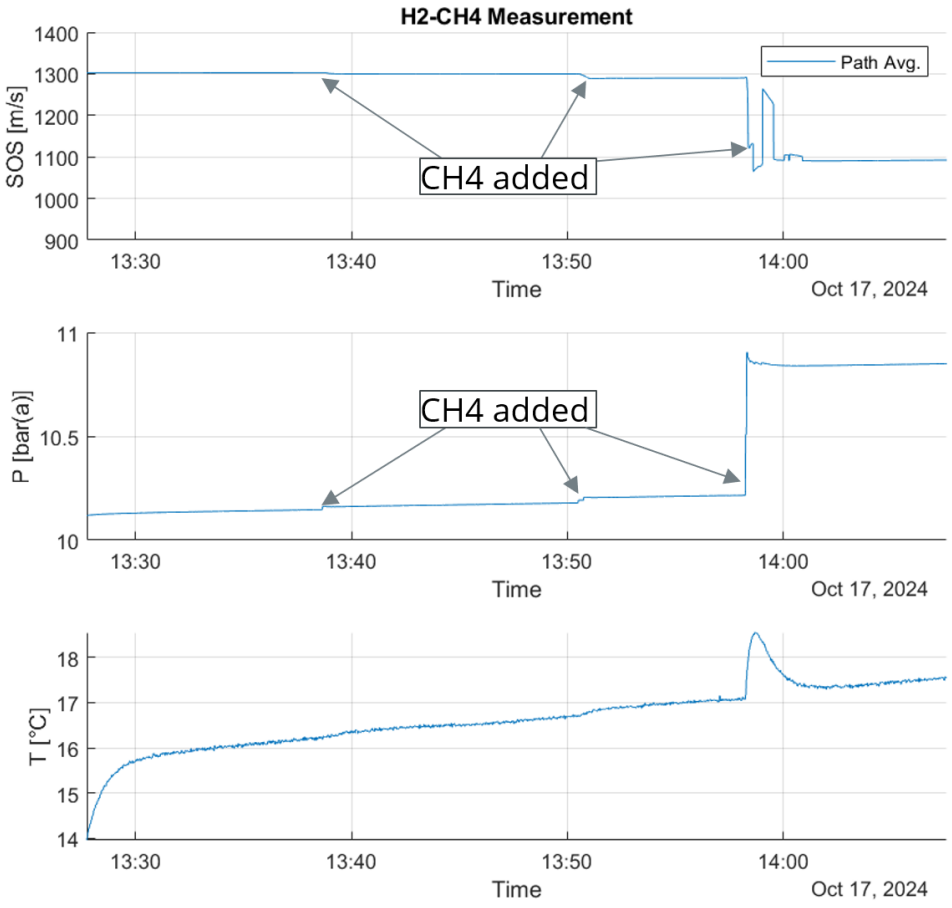

Figure 30: Measured SOS, p and T over the course of the H_2/CH_4 experiment.

Table 17: Reference molar fractions calculated via pressure change (H_2/CH_4).

Step	p_{before} $[bar(a)]$	Δp $[bar(a)]$	$frac_{H2}^{ref}$ $[mol\%]$	$frac_{CH4}^{ref}$ $[mol\%]$
0	-	-	>99.999	<0.001
1	10.1567	0.0119	99.883	0.117
2	10.1848	0.0245	99.644	0.356
3	10.2226	0.6184	93.960	6.040

Table 18: Results of the two H_2 purity algorithms denoted by the uppercase index "Mod." for the model-based algorithm and "Opt." for the optimization algorithm (H_2/CH_4).

Step	p_{USM} [$bar(a)$]	T_{USM} [$°C$]	SOS_{USM} [m/s]	$frac_{H2}^{Mod.}$ [$mol\%$]	$frac_{H2}^{Opt.}$ [$mol\%$]
0	10.146	16.21	1302.71	99.97	99.97
1	10.178	16.69	1299.74	99.88	99.88
2	10.215	17.07	1289.92	99.63	99.64
3	10.849	17.54	1092.23	93.88	93.89

Table 19: Deviation of the two H_2 purity algorithms to the reference molar fractions calculated via pressure change (H_2/CH_4).

Step	$Deviation_{H2}^{Mod.}$ [$mol\%$]	$Deviation_{H2}^{Opt.}$ [$mol\%$]
0	-0.030	-0.030
1	-0.003	-0.003
2	-0.014	-0.004
3	-0.08	-0.07

5. Conclusions

This deliverable investigates the impact of impurities in hydrogen on the flow measurement accuracy of calibrated flow rate meters. Three types of flow measurements devices were investigated:

- Mass Flow meter (MFM)
- Area Flow Meter (AFM)
- Differential Pressure Meter with Orifice Plate

The MFM, AFM and orifice plate were tested in the RWTH-IOB laboratory. Hydrogen was mixed with various impurities, including CH_4, O_2, N_2, CO, CO_2 and H_2O at concentrations up to 2 vol%. The measured flows of hydrogen mixtures with impurities were then compared to those of pure hydrogen across three volume flow rates corresponding to power outputs of 16 kW, 20 kW and 24 kW.

The results indicate that the MFM offers the highest accuracy among the three devices tested. It consistently achieves deviations below 2.5% of the expected volume flow, regardless of the type of impurity present. This high level of accuracy can be attributed to its measurement method based on heat capacity, which is minimally affected by the addition of impurities.

In contrast, both the AFM and Orifice Plate exhibited significantly higher deviations from expected volume flows. The extent of this deviation closely correlates with the density of the gas mixture. As the density increases due to added impurities, so does the deviation from expected values. Specifically, the AFM showed deviations up to 16%, while the Orifice Plate reached up to 20% when CO_2 was added as an impurity.

Operating these devices without any adjustments could lead to substantial misestimations of actual flow rates. The results demonstrate that even small amounts of impurities (up to 2 vol%) can significantly affect both the AFM and Orifice Plate's performance. However, applying a correction factor that accounts for changes in mixture density relative to pure hydrogen reduced deviations to a maximum of 4.1%. It is important to note that this correction method requires accurate knowledge about the density of the specific hydrogen mixture being measured.

Additionally, impurities also influenced pollutant emissions and off-gas composition of the combustion. Notably, O_2 and CH_4 as impurities had significant impacts on these results. The addition of O_2 as an impurity led to an increase in oxygen content in the off-gas by up to 4 vol% and increased NO_x emissions by 32-37%. In contrast, adding CH_4 resulted in a decrease in oxygen concentration to between 1.7-2 vol% and reduced NO_x emissions by 13-15%. For comparison, when using pure hydrogen, the oxygen content was approximately 3 vol%. Furthermore, the addition of impurities containing carbon lead to a slight increase in CO and CO_2 concentration in the off-gas.

In parallel, experimental investigations of an Ultrasonic Flow Meter (USM) were conducted at SIEN to estimate the purity of hydrogen. Since the Speed of Sound (SOS) in hydrogens is significantly reduced when impurities are added, comparing the SOS measured by the USM with the expected SOS of pure hydrogen can help estimate the molar fractions of hydrogen of a known impurity gas.

To achieve this, SIEN developed two algorithms for estimating H_2 purity using measurement of SOS, temperature and pressure of the fluid. The first algorithm employs two easy to compute pre-trained models, while the second algorithm uses a suitable equation of state (EOS) for gas mixtures, e.g., GERG-2008. Both algorithms function by analyzing the deviation between measured SOS and that of pure hydrogen to calculate the mole fraction of hydrogen and impurities. The uncertainty of these algorithms was assessed through numerical simulations and was found to range from 0.03 mol% to 0.09 mol%, depending on the impurity gas used.

Experimental testing of the algorithms was carried out at SIEN facilities using a prototype USM designed for pure hydrogen, under static conditions – meaning there was no actual fluid flow during measurements. Nitrogen (N_2) and Methane (CH_4) were investigated as impurity gases at concentrations up to 2.3 mol% and 6.04 mol%, respectively. Both algorithms performed as expected, and the measurement results were in excellent agreement with the numerical simulations.

6. References

[1] ABB Automation Products GmbH: Industrial Flow Measurement - Basics and Practice, Zurich, Switzerland, 2017.

[2] Aerodynamic Measurements, Elsevier, 2011.

[3] Bird, J. O.; Chivers, P. J.: Measurement of fluid flow, in: Newnes Engineering and Physical Science Pocket Book, Elsevier, 1993, pp. 370–381.

[4] Christian Bürkert GmbH & Co. KG: Direct-acting 2/2-way plunger valve - Type 6027 - Data Sheet, 2023.

[5] Christian Bürkert GmbH & Co. KG: Mass Flow Controller / Mass Flow Meter for gases - Type 8742 - Data Sheet, 2024.

[6] Christian Bürkert GmbH & Co. KG: Servo-assisted 2/2-way diaphragm valve - Type 0290 - Data Sheet, 2024.

[7] DIN EN 60584-1:2014-07: Thermocouples - Part 1: EMF specifications and tolerances, Deutsches Institut für Normung e. V., 2014.

[8] DIN EN 17124:2022-12: Hydrogen fuel - Product specification and quality assurance for hydrogen refuelling points dispensing gaseous hydrogen - Proton exchange membrane (PEM) fuel cell applications for vehicles, Deutsches Institut für Normung e. V., 2022.

[9] DIN EN ISO 5167-1:2022: Measurement of fluid flow by means of pressure differential devices inserted in circular cross-section conduits running full - Part 1: General principles and requirements, Deutsches Institut für Normung e. V., 2022.

[10] DIN EN ISO 5167-2:2022: Measurement of fluid flow by means of pressure differential devices inserted in circular cross-section conduits running full - Part 2: Orifice plates, Deutsches Institut für Normung e. V., 2022.

[11] Dutton, F. B.: Dalton's law of partial pressures, in: Journal of Chemical Education (1961), No. 8, A545, DOI: 10.1021/ed038pA545.1.

[12] Elgas: User manual for pressure transducer EDT 96, URL: https://www.elgas.cz/en/digital-pressure-transmitter-edt-23, abgerufen am: 06.12.2024.

[13] Elster GmbH: Burner control unit for PROFIBUS-DP BCU 400.B1 - Technical Information, 2011.

[14] Elster GmbH: Burners with ceramic tube BIC, BICA, BICW, ZIC, ZICW - Technical Information, 2017.

[15] Elster GmbH: Pressure gauges KFM, RFM - Technical Information, 2020.

[16] Elster GmbH: Pressure switches for gas DG - Technical Information, 2021.

[17] Elster GmbH: Solenoid valves for gas VAS, double solenoid valves VCS - Technical Information, 2023.

[18] Elster GmbH: UV sensors UVS 5, UVS 10 - Technical Information, 2023.

[19] Fowles, G.; Boyes, W. H.: Measurement of Flow, in: Instrumentation Reference Book, Elsevier, 2010, pp. 31–68.

[20] FPZ Side channel blowers Flyer (2024) (2024).

[21] Gätke, J.: Akustische Strömungs-und Durchflussmessung, Akad.-Verlag, 1991.

[22] Georg Rollmann: Calculation of correction factors for variable area flow meters at deviating working conditions (2019).

[23] German Association for Gas and Water (DVGW e.V.): Technical Rule DVGW G260 - Gas Quality, 2021.

[24] Godula-Jopek, A.: Introduction, in: Godula-Jopek, A., Stolten, Detlef (Hrsg.): Hydrogen production by electrolysis, 1st edition, Weinheim, Wiley-VCH, 2015, pp. 1–31.

[25] **halstrup-walcher GmbH:** Differential pressure transmitter P34 - Data Sheet, 2023.

[26] **Höntzsch GmbH & Co. KG:** Thermal flow sensor TA Di with integrated measuring transducer - Data Sheet, 2024.

[27] **ISO/IEC Guide 98-3:2008:** Uncertainty of measurement - Part 3: Guide to the expression of uncertainty in measurement (GUM:1995), International Organization for Standardization.

[28] **ISO 14687:2019:** Hydrogen fuel quality - Product specification, International Organization for Standardization, 2019.

[29] **ISO 13577-2:2021:** Industrial furnaces and associated processing equipment - Safety - Part 2: Combustion and fuel handling systems, International Organization for Standardization, 2021.

[30] **ISO/TR 15377:2023:** Measurement of fluid flow by means of pressure-differential devices - Guidelines for the specification of orifice plates, nozzles and Venturi tubes beyond the scope of ISO 5167 series, International Organization for Standardization, 2023.

[31] **Krohne Messtechnik GmbH:** Variable area flowmeter - H250 M40 - Technical Datasheet, 2022.

[32] **Kunz, O.; Wagner, W.:** The GERG-2008 Wide-Range Equation of State for Natural Gases and Other Mixtures: An Expansion of GERG-2004, in: Journal of Chemical & Engineering Data (2012), No. 11, pp. 3032–3091, DOI: 10.1021/je300655b.

[33] Measurement and Instrumentation, Elsevier, 2016.

[34] Measurement and Instrumentation, Elsevier, 2021.

[35] **Michell Instruments Ltd.:** Easidew Transmitters, 2021.

[36] **Pfeifer, H.; Nacke, B.; Beneke, F.:** Praxishandbuch Thermoprozesstechnik: Band I: Grundlagen-Prozesse-Verfahren, Vulkan, 2009.

[37] **SIREN, K. A.; ROSÉN, G.; VAD, J.; NIELSEN, P. V.:** EXPERIMENTAL TECHNIQUES, in: Industrial Ventilation Design Guidebook, Elsevier, 2001, pp. 1105–1195.

[38] **Tränkler, H.-R.; Reindl, L. (Hrsg.):** Sensortechnik, Berlin, Heidelberg, Springer Berlin Heidelberg, 2014.

[39] **Ullmann, F.:** Gas quality measurement of gas mixtures containing hydrogen with ultrasonic flow meters - experiences, challenges and perspectives, in: 2022 IEEE 12th Sensor Array and Multichannel Signal Processing Workshop (SAM), 2022 IEEE 12th Sensor Array and Multichannel Signal Processing Workshop (SAM), Trondheim, Norway, 20.06.2022 - 23.06.2022, IEEE, 2022, pp. 51–55.

[40] **Wiegleb, G.:** Feuchtemessung in Gasen, in: Wiegleb, G. (Hrsg.): Gasmesstechnik in Theorie und Praxis, Wiesbaden, Springer Fachmedien Wiesbaden, 2016, pp. 575–624.

[41] **Wiegleb, G.:** Flow Measurement Technology, in: Wiegleb, G. (Hrsg.): Gas Measurement Technology in Theory and Practice, Wiesbaden, Germany, Springer Fachmedien Wiesbaden, 2023, pp. 631–682.

[42] **Wiegleb, G. (Hrsg.):** Gas Measurement Technology in Theory and Practice, Wiesbaden, Germany, Springer Fachmedien Wiesbaden, 2023.

[43] **WIKA Alexander Wiegand SE & Co. KG:** Pressure transmitter for general industrial applications - Model A-10 - Data Sheet, 2023.

Get in touch

Website

http://hyinheat.eu/

Email address

info@hyinheat.eu